“© 2022 IEEE. Personal use of this material is permitted. Permission from IEEE must be obtained for all other uses, in any current or future media, including reprinting/republishing this material for advertising or promotional purposes, creating new collective works, for resale or redistribution to servers or lists, or reuse of any copyrighted component of this work in other works.”

Integrating Low-Complexity and Flexible Sensing into Communication Systems

Kai Wu, J. Andrew Zhang, *Senior Member, IEEE*, Xiaojing Huang, *Senior Member, IEEE*, and Y. Jay Guo, *Fellow, IEEE*

***Abstract*—Integrating sensing into standardized communication systems can potentially benefit many consumer applications that require both radio frequency functions. However, without an effective sensing method, such integration may not achieve the expected gains of cost and energy efficiency. Existing sensing methods, which use communication payload signals, either have limited sensing performance or suffer from high complexity. In this paper, we develop a novel and flexible sensing framework which has a complexity only dominated by a Fourier transform and also provides the flexibility in adapting to different sensing needs. We propose to segment a whole block of echo signal evenly into sub-blocks; adjacent ones are allowed to overlap. We design a virtual cyclic prefix (VCP) for each sub-block that allows us to employ two common ways of removing communication data symbols and generate two types of range-Doppler maps (RDMs) for sensing. We perform a comprehensive analysis of the signal components in the RDMs, proving that their interference-plus-noise (IN) terms are approximately Gaussian distributed. The statistical properties of the distributions are derived, which leads to the analytical comparisons between the two RDMs as well as between the prior and our sensing methods. Moreover, the impact of the lengths of sub-block, VCP and overlapping signal on sensing performance is analyzed. Criteria for designing these lengths for better sensing performance are also provided. Extensive simulations validate the superiority of the proposed sensing framework over prior methods in terms of signal-to-IN ratios in RDMs, detecting performance and flexibility.**

***Index Terms*—Integrated sensing and communications (ISAC), joint communications and sensing (JCAS), dual-function radar communications (DFRC), OFDM, DFT-spread OFDM, orthogonal time-frequency space (OTFS), CP, range-Doppler map (RDM)**

I. Introduction

Integrated sensing and communications (ISAC) has attracted extensive attention recently. By allowing sensing and communications to share the same waveform, hardware and frequency spectrum etc., ISAC not only improves cost and energy efficiency but also helps alleviate the increasingly severe congestion of frequency spectrum [1]. As popularly seen in the literature, ISAC designs can be sensing-centric (SC) [2]–[5], communication-centric (CC) [6]–[11] and joint-design [12]–[16]. While SC (or CC) adds communications (or sensing) into existing sensing (or communications) systems as a secondary function, a joint-design ISAC generally solves a holistically formulated optimization problem for a (sub-)optimal dual-function waveform [17]–[19]. In this paper, we focus on CC-ISAC which can potentially expedite the market penetration of ISAC into consumer markets [20]. Moreover, CC-ISAC considered here performs active sensing; c.f., passive sensing based on communication signals.

TABLE I: Commonly used acronyms througout the paper

Acronym.	Description
CA-CFAR	cell-averaging constant false-alarm rate detector
CCC	Cyclic cross-correlation
CC-ISAC	Communication-centric ISAC
COS	Classical OFDM sensing
C-COS	CCC-based COS
CP; RCP; VCP	cyclic prefix; reduced CP; virtual CP
DFT	Discrete Fourier transform
DFT-S-OFDM	DFT-spread OFDM
ISAC	Integrated sensing and communications
IN	Interference-plus-noise
OFDM	Orthogonal frequency-division multiplexing
OTFS	Orthogonal time-frequency space
RDM	Range-Doppler map
SINR	signal-to-IN ratio

A widely studied issue of CC-ISAC is how to achieve satisfactory sensing performance based on standardized communication waveforms. Orthogonal frequency-division multiplexing (OFDM) and its variant waveforms are popular in CC-ISAC. Note that sensing here is similar to the conventional radar sensing, i.e., detecting targets and estimating their parameters (mostly location and velocity) from the echo signals. In [10], OFDM waveform-based sensing is developed. The method has been widely studied since its development; see [21], [22] and their references. Thus, we call it the classical OFDM sensing (COS). In short, COS i) transforms a block of OFDM symbols into the frequency domain; ii) removes communication data symbols through a point-wise division; iii) takes a two-dimensional DFT to generate a so-called range-Doppler map (RDM); and iv) performs target detection and estimation using the RDM. COS will be further reviewed in Section II-B using our signal model.

In [11], a COS-like sensing method is developed for discrete Fourier transform (DFT)-spread OFDM (DFT-S-OFDM) waveforms. Different from OFDM, DFT-S-OFDM presents Gaussian randomness in the frequency domain. Hence, directly dividing communication data symbols can severely amplify noise background. To this end, the cyclic cross-correlation (CCC) is introduced in [11] to replace the steps i) and ii) of COS. For convenience, let us call the method developed in [11] as C-COS. Note that C-COS can be employed for sensing based on the orthogonal time-frequency space (OTFS) which is a potential waveform candidate for future mobile

This work is partially supported by the Australian Research Council under the Discovery Project Grant DP210101411.

K. Wu, J. A. Zhang, X. Huang and Y. J. Guo are with the Global Big Data Technologies Centre, University of Technology Sydney, Sydney, NSW 2007, Australia (e-mail: kai.wu@uts.edu.au; andrew.zhang@uts.edu.au; xiaojing.huang@uts.edu.au; jay.guo@uts.edu.au).

communications [23]. While using C-COS requires OTFS to be cyclic prefixed for each symbol as in OFDM and DFT-S-OFDM, OTFS with a reduced cyclic prefix (RCP), i.e., a single cyclic prefix (CP) for the whole block of OTFS symbols, is the main trend in the OTFS literature.

For RCP-OTFS, COS and C-COS cannot be directly applied. So far, RCP-OTFS sensing is mainly based on the maximum likelihood detection (MLD). In [24], an MLD problem for RCP-OTFS sensing is formulated in the delay-Doppler domain. In the case of a single target, solving an MLD can be done through a matched filter. This is performed in [25] and [26]. In [27], an MLD problem for RCP-OTFS sensing is formulated in the time domain which, as claimed therein, provides more insight compared with the MLD in the delay-Doppler domain. Regardless of the domains used for formulating MLD problems, solving them requires an exhaustive search over the whole range-Doppler region. For each range-Doppler grid to be tested, a metric is calculated with high-dimensional matrix operations involved. In addition, solving the MLD problems requires a set of high-dimensional channel matrices which are pre-generated over the range-Doppler grids to be searched. Storing these matrices and accessing them in real time can be challenging in practice.

In this paper, we develop a novel sensing framework that can be used for either waveforms with regular CPs, like OFDM and DFT-S-OFDM, or waveforms with RCP, like RCP-OTFS. The new sensing framework has a similar complexity to COS yet with enhanced sensing flexibility and performance. Our key innovations are illustrated below.

1) We propose a sensing framework that divides a block of signal evenly into multiple sub blocks. Unlike most existing schemes, such as COS, we do not follow the underlying communication system but instead allow the number of samples in each sub-block to be different from that in a communication symbol. Moreover, we allow consecutive sub-blocks to overlap, which introduces a new flexibility to optimize the sensing performance as well as to balance performance and implementation overhead.
2) We propose a virtual CP (VCP) that allows us to turn the echo signal in each sub-block into a sum of scaled and cyclically-shifted versions of a known signal. This then allows us to remove the communication data symbols in the frequency domain and generate RDMs, as done in COS or C-COS. Moreover, the duration of the proposed VCP can be flexibly adjusted according to the maximum sensing distance. Such flexibility is not owned by COS and its variants, as they strictly follow the underlying communication system. Further, it is worth noting that the flexibility of the proposed VCP also lies in that it can be adjusted for better sensing performance.
3) We provide a comprehensive analysis of the interference-plus-noise (IN) terms of the RDMs obtained under the proposed sensing framework. We prove that the IN terms in both RDMs approximately conform to Gaussian distributions. The statistical properties of the distributions are also derived. Moreover, we derive the signal-to-IN ratios (SINRs) of both RDMs and extrapolate the results to COS and C-COS. Further, we provide a holistic comparison between COS and the proposed sensing framework for both RDMs. The performance of the proposed sensing framework under the two RDMs is also analytically compared.

Extensive simulations are provided to validate the proposed sensing framework and our analysis. In particular, we demonstrate that, as consistent with our analysis, the proposed sensing framework always outperforms COS and C-COS in low SNR regions where the upper limit of the region also matches the analytical result. We also confirm that the RDM obtained using CCC, as in C-COS [11], has a greater SINR than the RDM obtained based on the point-wise division, as in COS [10], in low SNR regions; however, the former outperforms the later in high SNR regions. While the low-SNR observation is consistent with the results in [11], the high-SNR result is unveiled for the first time. The critical value differentiating low and high SNR regions is also derived.

We remark that sensing based on standardized communication waveforms can also be performed using preambles. In [6], [7], different sensing methods are developed using the Golay complementary sequences (GCSs) in the preamble of IEEE 802.11ad communication signals. In [8], the Doppler resilience of IEEE 802.11ad-based sensing is improved by incorporating Prouhet-Thue-Morse sequences in the preamble. While these methods exploit the superb auto-correlation feature of GCSs for a high ranging performance, it can be non-trivial to adapt them for other communication standards. Moreover, as stated in [11], using a whole block of communication signal for sensing can be more robust to interference and noise compared with only using preambles. This paper is devoted to developing a flexible sensing framework that can be applied to most, if not all, communication systems. Thus, we use the payload signals as in COS and C-COS. The comparison between preamble- and payload-based sensing is out of the scope of this work. In fact, as they both have some unique advantages, their combination can be an interesting future work.

II. Signal Model and Problem Statement

In this section, the signal model of the considered ISAC scenario is first established based on the OTFS modulation. Then, COS is briefly reviewed. This further elicits several important issues that have not been effectively solved yet. Solutions to the issues will be developed in sequential sections.

A. Signal Model

We consider that a communication-only node is turned into an ISAC node by incorporating a sensing receiver. The communication signals are transmitted; meanwhile, the receiver collects target echo for sensing. As in most CC-ISAC work [6], [7], [10], [11], we ignore the self-interference, i.e., the signal leakage directly from the transmitter to the receiver, due to the implicit full-duplex operation. As for the communication waveform, we consider the OTFS modulation, not only because it is a potential waveform candidate for future mobile communications [23], but also due to its capability in representing other common multi-carrier waveforms, e.g., OFDM and DFT-S-OFDM.

Let d_i $(i = 0, 1, \cdots, I-1)$ denote the data symbols to be transmitted, where the data symbols are independently drawn from the same constellation, e.g., 64-QAM, and I denotes the total number of data symbols. In OTFS modulation, the I data symbols are first placed in a two-dimensional delay-Doppler plane. Let the delay and Doppler dimensions be discretized into M and N grids, respectively. Denoting the time duration of M data symbols as T, the sampling frequency along the Doppler dimension is then $\frac{1}{T}$, which leads to a Doppler resolution of $\frac{1}{NT}$. Since there are M grids along the delay dimension, the corresponding resolution is $\frac{T}{M}$. In the OTFS modulation, the data symbols can be mapped from the delay-Doppler domain into the frequency-time domain via the following transform [28],

$$S[m,n] = \frac{1}{\sqrt{MN}} \sum_{k=0}^{N-1} \sum_{l=0}^{M-1} d_{kM+l} e^{\mathrm{j}2\pi(\frac{nk}{N} - \frac{mT}{M} l\Delta_f)} \quad (1)$$

where j denotes the imaginary unit. Note that frequency and time are the dual domains of delay and Doppler, respectively.

The frequency-time-domain signal $S[m,n]$ is then transformed into the time domain by performing the IDFT w.r.t. m for each n. This leads to

$$s[l,n] = \sum_{m=0}^{M-1} S[m,n] \mathcal{Z}_M^{-ml}, \ \forall n, \quad (2)$$

where $\mathcal{Z}_M^{-ml}$ denotes the DFT basis, as given by

$$\mathcal{Z}_a^{bc} = e^{-\mathrm{j}\frac{2\pi bc}{a}} / \sqrt{a}. \quad (3)$$

If the critical sampling is employed, which is typical in practice, then $T\Delta_f$ in (1) becomes one and moreover the IDFT performed in (2) will cancel the l-related transform in (1). Treating l as the row index and n the column index, the signal $s[l,n]$ will be transmitted column-by-column and in each column the entries $l = 0, 1, \cdots, M-1$ are transmitted sequentially. Before going through the digital-to-analog converter, some extra processing on $s[l,n]$ would be necessary. To prevent the inter-symbol interference (ISI), cyclic prefix is generally used in multi-carrier transmissions. There are two types of CP in the OTFS literature.

In the first type, every M data symbols have a CP added [29], which is referred to as CP-OTFS hereafter. Let Q denote the number of samples in a CP. Based on $s[l,n]$ given in (2), the signal to be transmitted can be given by

$$\tilde{s}_{\mathrm{CP}}[i] = s\left[\left\langle \langle i \rangle_{M+Q} - Q \right\rangle_M, \lfloor i/(M+Q) \rfloor\right], \quad i = 0, 1, \cdots, N(M+Q)-1, \quad (4)$$

where $\langle x \rangle_y$ takes x modulo y and $\lfloor x \rfloor$ rounds toward negative infinity. The indexes on the RHS of (4) indicate that every $(M+Q)$ samples of $\tilde{s}_{\mathrm{CP}}[i]$ are obtained by copying the last Q samples from $s[0,n], s[1,n], \cdots, s[M-1,n]$ at some n and pasting to the beginning.

In the second-type CP, the whole block of MN data symbols have a single CP added, which is known as the reduced CP-OTFS (RCP-OTFS) [30]. The signal to be transmitted in RCP-OTFS can be given by

$$\tilde{s}_{\mathrm{RCP}}[i] = s\left[\langle \tilde{i} \rangle_M, \lfloor \tilde{i}/M \rfloor\right], \quad \text{s.t. } \tilde{i} = \langle i - Q \rangle_{MN}, \ i = 0, 1, \cdots, MN+Q-1, \quad (5)$$

where the indexes on the RHS indicate that the last Q samples from $s[0,N-1], s[1,N-1], \cdots, s[M-1,N-1]$ are copied and pasted to the beginning of $s[l,0]$. The CP-added signal will go through a digital-to-analog conversion (DAC) and other analog-domain processing, e.g., frequency up-conversion and power amplification etc., before being transmitted. A pulse-shaping filter is generally performed to reduce the out-of-band (OOB) emission. For illustration convenience, we do not include the filter in the signal model. Nevertheless, practical pulse-shaping filters will be used in our simulations.

As mentioned earlier, we consider a sensing receiver co-located with the communication transmitter. Therefore, it is reasonable to assume prefect synchronization and zero frequency offset for sensing. Consider P targets. The scattering coefficient, time delay and Doppler frequency of the p-th target are denoted by α_p, τ_p and ν_p, respectively. Let $\tilde{s}[i]$ be either $\tilde{s}_{\mathrm{CP}}[i]$ or $\tilde{s}_{\mathrm{RCP}}[i]$ (the set of i varies accordingly). The target echo, as a sum of the scaled and delayed versions of $\tilde{s}[i]$, can be modeled as

$$x[i] = \sum_{p=0}^{P-1} \tilde{\alpha}_p \tilde{s}\left[i - \mathsf{l}_p\right] e^{\mathrm{j}2\pi i \tilde{\mathsf{k}}_p} + w[i], \quad \text{s.t. } \tilde{\alpha}_p = \alpha_p e^{-\mathrm{j}2\pi\nu_p\tau_p}; \ \mathsf{l}_p = \tau_p/T_{\mathrm{s}}; \ \tilde{\mathsf{k}}_p = \nu_p T_{\mathrm{s}}, \quad (6)$$

where T_{s} is the sampling interval, and $w[i] \sim \mathcal{CN}\left(0, \sigma_w^2\right)$ is the additive noise conforming to a circularly-symmetric complex centered Gaussian distribution.

Remark 1: Some features of the above signal model are remarked here. *First*, the signal $\tilde{s}_{\mathrm{CP}}[i]$ can represent DFT-S-OFDM and OFDM with slight changes made on $S[m,n]$. In particular, DFT-S-OFDM can be obtained when the Fourier transform w.r.t. k is suppressed in (1), while OFDM is obtained when both Fourier transforms in (1) are skipped. *Second*, $s[l,n]$ obtained in (2) approximately conforms to a complex centered Gaussian distributions, as denoted by $s[l,n] \sim \mathcal{CN}(0, \sigma_d^2)$, where σ_d^2 is the power of d_i; see (1). The above result can be attained using (1) and (2) in combination with another two facts: the complex envelope of an uncoded OFDM system converges in distribution to a complex Gaussian random process [31]; the unitary DFT does not change the statistical properties and the whiteness of a Gaussian process [32]. *Third*, we can use the above two facts to validate that $s[l,n] \sim \mathcal{CN}(0, \sigma_d^2)$ also holds for DFT-S-OFDM and OFDM.

B. Classical OFDM Sensing (COS)

COS was developed about a decade ago and has been widely used in the sensing literature; see [21], [22] and their references. However, there are still some issues that have not been effectively solved yet. Below, we briefly review COS and highlight the issues. As COS is originally developed for CP-OFDM, we assume that $\tilde{s}_{\mathrm{CP}}[i]$ is transmitted and use $x[i]$ to describe the method.

In COS, the $(M+Q)N$ numbers of echo samples $x[i]$ are divided into N consecutive symbols, each having $(M+Q)$ samples. Removing the first Q samples in each symbol and taking the M-point unitary DFT of the remaining samples in the symbol, we obtain a common echo signal model

$$X_n[m] \approx \sum_{p=0}^{P-1} \tilde{\alpha}_p d[m,n] e^{-\mathrm{j}\frac{2\pi m \mathsf{l}_p}{M}} e^{\mathrm{j}2\pi n(M+Q)\tilde{\mathsf{k}}_p} + W_n[m],$$
$$\text{s.t. } d[m,n] = d_{kM+l}\big|_{l=0,k=n} \tag{7}$$

where d_{kM+l} as given in (1) is a data symbol drawn from the communication constellation, and $W_n[m]$ denotes the DFT of the background noise. Note that, as often done in radar signal processing [33], the intra-symbol Doppler effect is suppressed in (7).

Dividing $X_n[m]$ by $S[m,n]$ in a point-wise manner, we can remove the communication data symbols. Then, a two-dimensional Fourier transform can be performed over m and n, leading to the following RDM,

$$\begin{aligned} U_k^{\mathrm{r}}[l] &= \sum_{n=0}^{N-1}\sum_{m=0}^{M-1} X_n[m] \Big/ S[m,n] \mathcal{Z}_M^{-ml} \mathcal{Z}_N^{nk}, \\ &= \sum_{p=0}^{P-1} \tilde{\alpha}_p \mathcal{S}_M\left(l-\mathsf{l}_p\right) \mathcal{S}_N\left((M+Q)N\tilde{\mathsf{k}}_p - k\right) + W_k^{\mathrm{r}}[l], \end{aligned} \tag{8}$$

where the superscript $\{\cdot\}^{\mathrm{r}}$ stands for 'ratio' to differentiate with another way of removing $S[m,n]$, as to be illustrated in Section II-C3; $\mathcal{Z}_a^{bc}$ is the unitary DFT basis and defined in (3); $W_k[l]$ is the two-dimensional Fourier transform of $W_n^{\mathrm{r}}[m] \Big/ S[m,n]$; and $\mathcal{S}_x(y)$ is introduced to denote the DFT results of the two exponential signals in (7). The general form of $\mathcal{S}_x(y)$ is given by

$$\mathcal{S}_x(y) = \frac{1}{\sqrt{x}} \frac{\sin\left(\frac{x}{2}\frac{2\pi y}{x}\right)}{\sin\left(\frac{1}{2}\frac{2\pi y}{x}\right)} e^{\mathrm{j}\frac{x-1}{2}\frac{2\pi y}{x}}. \tag{9}$$

The function $\mathcal{S}_x(y)$ is localized around $y=0$ and hence $|Y_k[l]|$ can present P dominant peaks in the range-Doppler domain, if $\tilde{\alpha}_p \ \forall p$ is sufficiently large. Thus, a threshold detector based on, e.g., likelihood ratio test (LRT), can be developed for target detection, from which coarse estimations of target parameters can also be attained.

C. Motivation and Problem Statement

COS has been widely applied given its low complexity. However, COS and many of its variants can have limited sensing performance, as they follow the underlying communication systems. Some intriguing issues are illustrated below.

1) CP-limited sensing distance: CP plays a non-trivial role in COS. Specifically, CP makes each received symbol consists of cyclically shifted version of the transmitted symbol. This then enables us to attain the convenient echo model given in (7) and further facilitates the removal of $S[m,n]$ to generate the RDM given in (8). However, CP also puts a constraint on sensing. Namely, the round-trip delay of the maximum sensing distance should be smaller than the time duration of the CP. Such limitation stands even when we have a sufficient link budget for sensing a longer distance. Moreover, for the communication waveform with a reduced CP, as modeled in (5), COS is not directly applicable.

2) Communication-limited velocity measurement: While the sensing distance is limited by CP, the velocity measurement performance can be constrained by the values of M and N. Substituting $\tilde{k}_p = \nu_p T_{\mathrm{s}}$ into (7), we see that the Doppler frequency ν_p becomes the frequency of the exponential signal of n and $(M+Q)T_{\mathrm{s}}$ is the sampling interval. Thus, the maximum (unambiguous) measurable value of the Doppler frequency, as denoted by $\nu_{\max}$, and its resolution, as denoted by Δ_ν, can be given by

$$\nu_{\max} = 1\Big/\big(2(M+Q)T_{\mathrm{s}}\big);\ \Delta_\nu = 1\Big/\big(N(M+Q)T_{\mathrm{s}}\big).$$

While a small M can give us a large unambiguous region for Doppler measurement, a large N is then necessary to keep a small Δ_ν. However, assigning the values of M and N in a sensing-favorable way may degrade the performance of the underlying communication system, e.g., 5G [34], that generally has stringent requirements on the two parameters.

3) COS adapted for DFT-S-OFDM: As shown in (8), communication data symbols are removed via point-wise divisions in COS. For CP-OFDM, this is okay, as $S[m,n]$, directly drawn from a constellation, does not take zero in general. However, for DFT-S-OFDM and OTFS, $S[m,n]$ conforms to a complex centered Gaussian distribution, as illustrated in Remark 1. This means a certain portion of $S[m,n]$ is centered around the origin and the direct division can lead to severe noise enhancement. To address the issue, a time-domain CCC is proposed in [11] to replace the frequency-domain division. The RDM under CCC can be written based on (8), leading to

$$U_k^{\mathrm{c}}[l] = \sum_{n=0}^{N-1}\sum_{m=0}^{M-1} X_n[m] S^*[m,n] \mathcal{Z}_M^{-ml} \mathcal{Z}_N^{nk}, \tag{10}$$

where a closed-form result, as in the second line of (8), is not available, due to the randomness of $S^*[m,n]$. Note that $S[m,n]$ here is not the same as in (8). As said in Remark 1, for DFT-S-OFDM, $S[m,n]$ can be obtained by suppressing the k-related Fourier transform in (1). Now that we have two ways of generating RDMs, a question follows naturally: which one gives the better sensing performance?

It is worth noting that the issues highlighted in Sections II-C1 and II-C2 have barely been treated yet in the literature. As seen in [10], [11], [21], [22], COS and many of its variants often follow the underlying communication system w.r.t. M and N and assume by default that the maximum round-trip delay of sensing targets is no greater than the CP duration. For CP-OTFS with demodulation performed in the delay-Doppler domain, channel estimation, as developed in [29], is conceptually similar to target parameter estimation in sensing. However, this also makes sensing performance suffer from the communication-incurred constraints, as pointed out in Section. II-C1 and II-C2.

Moreover, the question asked in Section II-C3 has not been systematically investigated, although it was shown through simulations in [11] that the CCC-based RDM has better sensing performance than the ratio-based RDM in low SNR

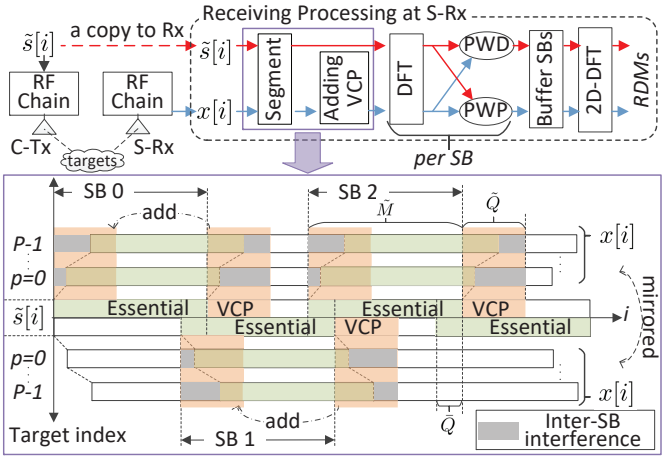

Fig. 1: The schematic diagram of the proposed sensing framework, where a sensing receiver (S-Rx) is co-located with a communication transmitter (C-Tx) and receives the echo signal $x[i]$ for wireless sensing. Substantially differentiating our design with previous ones, e.g., COS, is the highlighted block segmentation and virtual cyclic prefix (VCP). These operations turn the block of echo signal $x[i]$, as well as the copy of transmitted signal $\tilde{s}[i]$, into $\tilde{N}$ sub-blocks (SBs) each having $\tilde{M}$ samples. Afterwards, two common ways of generating RDMs, using point-wise division (PWD) [10] and product (PWP) [11], can be performed.

regions. This, however, is not always the case, as will be revealed in Section IV. To address the issues highlighted in Sections II-C1 and II-C2, we develop a novel flexible sensing framework in Section III. Performance analysis for the proposed sensing framework will be conducted in Section IV, which also answers the question asked in Section II-C3.

III. A Low-Complexity Sensing Framework

The proposed sensing framework is illustrated in Fig. 1. A communication transmitter (C-Tx) transmits $\tilde{s}[i]$ which can be either $\tilde{s}_{\rm CP}[i]$ in (4) with regular CPs (e.g., OFDM and DFT-S-OFDM) or $\tilde{s}_{\rm RCP}[i]$ in (5) with a RCP (e.g., RCP-OTFS). A copy of $\tilde{s}[i]$ is given to the sensing receiver (S-Rx), which, as mentioned earlier, co-locates with C-Tx and shares the same clock. While $\tilde{s}[i]$ is transmitted, S-Rx receives the target echo, i.e., $x[i]$ given in (6). The proposed sensing framework solely relies on $x[i]$ and $\tilde{s}[i]$ without requiring any cooperation or changes from C-Tx[1]. The sensing receiver starts with segmenting $x[i]$ and $\tilde{s}[i]$ into multiple consecutive sub-blocks, then removes or exploits the communication data symbols for generating an RDM. Substantially differentiating the proposed sensing framework from previous sensing methods, e.g., COS, is the way a block of samples is segmented, as detailed next.

Unlike previous designs fully complying with the underlying communication systems, we proposed to segment $x[i]$ into $\tilde{N}$ sub-blocks, each having $\tilde{M}$ samples, where $\tilde{N} = N$ is not required in our design. Moreover, we allow the consecutive sub-blocks to overlap by $\bar{Q}$ samples, where $\bar{Q}$ is either zero or a positive integer. As also shown in Fig. 1, we segment the communication-transmitted signal $\tilde{s}[i]$, *a copy at the sensing receiver*, in the same way as described above and call each segment the essential signal of the sub-block. Due to the propagation delay of a target, part of the essential signal is not within the received sub-block but right after it. To preserve the essential signal in each sub-block, we propose to add the $\tilde{Q}$ samples right after a sub-block onto the first $\tilde{Q}$ samples within the sub-block, creating a VCP. Note that VCPs are samples from the block of received echo signals with fixed and known positions. Also note that VCP is independent from the original CP of the underlying communication system. It is only introduced for sensing receiver and will not incur any change to the communication transmitter.

As seen from Fig. 1, adding VCP can make each received sub-block comprised of cyclically shifted versions of its essential signal part, as long as $\tilde{Q}$, *not* Q *any more*, is greater than the maximum target delay. Since the value of $\tilde{Q}$ is not limited to the original CP length Q, we can design the maximum sensing distance flexibly subject to a sufficient link budget. Next, the above description is further elaborated on using the signal model provided in Section II.

Let $s_n[l]$ denote the essential signal of the n-th sub-block. Based on the above illustration, we can write $s_n[l]$ as

$$s_n[l] = \tilde{s}[n(\tilde{M}-\bar{Q})+l],\ l = 0, 1, \cdots, \tilde{M}-1,$$
$$n = 0, 1, \cdots, \tilde{N}-1,\ \tilde{N} = \left\lfloor \frac{(I-\tilde{Q}-\bar{Q})}{(\tilde{M}-\bar{Q})} \right\rfloor, \quad (11)$$

where $\tilde{s}[\cdot]$ on the RHS can be either $\tilde{s}_{\rm CP}[i]$ in (4) or $\tilde{s}_{\rm RCP}[i]$ in (5) and $\tilde{N}$ is the total number of sub-blocks. Take the three sub-blocks in Fig. 1 for an illustration. By excluding the last $\bar{Q}$ samples of sub-block two and its $\tilde{Q}$-sample VCP, we see that each of the first three sub-blocks has $(\tilde{M}-\bar{Q})$ unique samples. This can be generalized into the expression of $\tilde{N}$ given in (11).

With reference to Fig. 1, after adding VCP, the received signal in sub-block n becomes

$$x_n[l] \approx \sum_{p=0}^{P-1} \tilde{\alpha}_p s_n\left[\langle l-\mathsf{l}_p\rangle_{\tilde{M}}\right] e^{\mathrm{j}2\pi n(\tilde{M}-\bar{Q})\tilde{\mathsf{k}}_p} + w_n[l] + z_n^{(p)}[l] g_{\tilde{Q}}[l],\ l = 0, 1, \cdots, \tilde{M}-1, \quad (12)$$

where $\tilde{\alpha}_p$, l_p and $\tilde{\mathsf{k}}_p$ are given in (6). Similar to (7), the approximation here is also due to the suppression of the intra-sub-block Doppler impact. We emphasize that, due to the $\bar{Q}$-sample overlapping of consecutive sub-blocks, the Doppler phase is $2\pi(\tilde{M}-\bar{Q})\tilde{\mathsf{k}}_p$ *not* $2\pi\tilde{M}\tilde{\mathsf{k}}_p$. In (12), $z_n^{(p)}[l] g_{\tilde{Q}}[l]$ denotes the interference term and $g_{\tilde{Q}}[l]$ is a rectangular window function which takes one at $l = 0, 1, \cdots, \tilde{Q}-1$, and zero elsewhere. Moreover, the noise term $w_n[l]$ in (12) is obtained by first segmenting $w[i]$ given in (6) as done in (11) and then adding VCP. Since the addition of two i.i.d. Gaussian variables is still Gaussian with the variance doubled, we have

$$w_n[l] \sim \begin{cases} \mathcal{CN}(0, 2\sigma_w^2) & \text{for } l = 0, 1, \cdots, \tilde{Q}-1 \\ \mathcal{CN}(0, \sigma_w^2) & \text{for } l = \tilde{Q}, \cdots, \tilde{M}-1 \end{cases}. \quad (13)$$

We notice that the interference term in (12) is the price paid for having VCP (i.e., sensing flexibility). Though the interference will make the white background noise become colored, we will show in Section IV that the overall interference-plus-noise background in the RDM still approximates a white Gaussian distribution under certain conditions.

[1]Since the proposed design does not affect the underlying communication system at all, we shall only focus on the sensing in this paper.

As in OFDM, the cyclic shift of the essential signal preserves the sub-carrier orthogonality. Therefore, taking the $\tilde{M}$-point DFT of $x_n[l]$ w.r.t. l leads to

$$X_n[m] = \sum_{p=0}^{P-1} \tilde{\alpha}_p S_n[m] e^{-\mathsf{j}\frac{2\pi m \mathsf{l}_p}{\tilde{M}}} e^{\mathsf{j}\frac{2\pi n \mathsf{k}_p}{\tilde{N}}} + W_n[m] + Z_n[m],$$
$$\text{s.t. } \mathsf{k}_p = \tilde{N}(\tilde{M} - \bar{Q})\tilde{\mathsf{k}}_p,$$
$$F_n[m] = \sum_{l=0}^{\tilde{M}-1} f_n[l] \mathcal{Z}_{\tilde{M}}^{lm}, \ (F, f) \in \{(S, s), (W, w)\},$$
$$Z_n[m] = \sum_{p=0}^{P-1} \tilde{\alpha}_p \sum_{l=0}^{\tilde{M}-1} z_n^{(p)}[l] g_{\bar{Q}}[l] \mathcal{Z}_{\tilde{M}}^{lm}, \tag{14}$$

where $S_n[m]$, $W_n[m]$ and $Z_n[m]$ are the DFTs of the respective terms in (12). We notice again that the unitary DFT basis, as defined in (3), is used. Since $s_n[l]$ is known, $S_n[m]$ can be readily calculated. Corresponding to (8), we can divide both sides of $X_n[m]$ by $S_n[m]$ and take the two-dimensional DFT w.r.t. n and m, attaining the following ratio-based RDM:

$$V_k^{\mathrm{r}}[l] = \sum_{p=0}^{P-1} \tilde{\alpha}_p \mathcal{S}_{\tilde{M}}(l - \mathsf{l}_p) \mathcal{S}_{\tilde{N}}(\mathsf{k}_p - k) + W_k^{\mathrm{r}}[l] + Z_k^{\mathrm{r}}[l],$$
$$\text{s.t. } \mathsf{X}_k^{\mathrm{r}}[l] = \sum_{n=0}^{N-1} \sum_{m=0}^{M-1} \frac{\mathsf{X}_n[m]}{S_n[m]} \mathcal{Z}_M^{-ml} \mathcal{Z}_N^{nk}, \ \mathsf{X} \in \{W, Z\} \tag{15}$$

where $\mathcal{S}_x(y)$ is defined in (9). Corresponding to (10), we can multiply both sides of $X_n[m]$ by the conjugate of $S_n[m]$ and take the same DFT w.r.t. n and m as above, obtaining the CCC-based RDM:

$$V_k^{\mathrm{c}}[l] = \sum_{p=0}^{P-1} \tilde{\alpha}_p S_k^{\mathrm{c}}[l] + W_k^{\mathrm{c}}[l] + Z_k^{\mathrm{c}}[l], \tag{16}$$
$$\text{s.t. } S_k^{\mathrm{c}}[l] = \sum_{n=0}^{\tilde{N}-1} \sum_{m=0}^{\tilde{M}-1} |S_n[m]|^2 e^{-\mathsf{j}\frac{2\pi m \mathsf{l}_p}{\tilde{M}}} e^{\mathsf{j}\frac{2\pi n \mathsf{k}_p}{\tilde{N}}} \mathcal{Z}_{\tilde{M}}^{-ml} \mathcal{Z}_{\tilde{N}}^{nk};$$
$$\mathsf{X}_k^{\mathrm{r}}[l] = \sum_{n=0}^{\tilde{N}-1} \sum_{m=0}^{\tilde{M}-1} \mathsf{X}_n[m] S_n^*[m] \mathcal{Z}_{\tilde{M}}^{-ml} \mathcal{Z}_{\tilde{N}}^{nk}, \ \mathsf{X} \in \{W, Z\}.$$

Remark 2: We remark that the CCC-based RDM is different from the ratio-based one, particularly when $S_n[m]$ has non-constant amplitudes over m. As pointed out in [11], $S_k^{\mathrm{c}}[l]$ is the CCC between $s_n[l]$ given in (11) and $x_n[l]$ given in (12). This can be readily shown by writing $|S_n[m]|^2 = S_n[m]S_n^*[m]$, replacing $S_n[m]$ with its DFT expression $\sum_{l'=0}^{M-1} s_n[l'] \mathcal{Z}_{\tilde{M}}^{l'm}$ and rewriting the remaining m-related summation. CCC is essentially equivalent to the matched filtering in conventional radar signal processing [33]. Thus, at a target delay, CCC will generate a peak, facilitating target detection and estimation.

Based on the RDMs obtained in (15) and (16), target detection and parameter estimation can be performed for various sensing applications. Note that developing methods for target detection and parameter estimation will be out of the scope of this study, as we focus on designing the framework and investigating the unsolved issues highlighted in Section II-C. Nevertheless, as will be proved in the next section, Propositions 1 and 2 in specific, the IN signals in both RDMs, i.e., $W_k^{\mathrm{r}}[l] + Z_k^{\mathrm{r}}[l]$ and $W_k^{\mathrm{c}}[l] + Z_k^{\mathrm{c}}[l]$, over range-Doppler grids, i.e., k and l, approximately conform to i.i.d. Gaussian distributions. This enables many existing target detectors and parameter estimators to be directly applicable under the proposed sensing framework. To validate the new design and analysis, the cell-averaging constant false-alarm rate detector (CA-CFAR) [33, Chapter 16] will be performed in our simulations.

TABLE II: Proposed Sensing Framework

Input: $\tilde{M}$, $\tilde{Q}$, $\bar{Q}$, $S_n[m]$ and $\tilde{N}$ given in (11), and $x[i]$ given in (6).

1) Segment $x[i]$ into $\tilde{N}$ sub-blocks (SBs): the n-th SB starts from the $n(\tilde{M} - \bar{Q})$ $(n = 0, 1, \cdots, \tilde{N} - 1)$ and has $\tilde{M}$ samples;
2) Add the $\tilde{Q}$ samples after each SB onto the first $\tilde{Q}$ within the SB;
3) Take the $\tilde{M}$-point DFT of each SB, attaining $X_n[m]$ given in (14);
4) If the ratio-based RDM is preferred, divide $X_n[m]$ by $S_n[m]$ pointwise and take a two-dimensional DFT w.r.t. n and m, leading to (15);
5) If the CCC-based RDM is chosen, multiply $X_n[m]$ with $S_n^*[m]$ pointwise and take a two-dimensional DFT, yielding (16);
6) Provided P_{F}, N_{g}^k, N_{g}^l, N_{r}^k and N_{r}^l, enumerate each range-Doppler grid by performing the following steps,
   a) Estimate the power of the local IN background according to (17);
   b) Calculate the detecting threshold T based on (18);
   c) If a power of the grid under test is greater than T, a target exists; otherwise, no target. If a target exists, the coarse estimates of its parameters can be obtained; see (19).

Next, we summarize the proposed sensing framework in Table II, where CA-CFAR is also briefly described. From the input of Table II, we see some extra parameters, e.g., $\tilde{M}$, $\tilde{Q}$ and $\bar{Q}$ that are not owned by COS. These parameters endow the proposed sensing framework with better flexibility and adaptability compared with COS. Their design criteria will be illustrated in Section IV. In Table II, Steps 1) to 2) perform the proposed block segmentation and VCP. Step 3) transforms the time-domain signal into the frequency domain. Steps 4) and 5) show two different ways of removing communication data symbols and accordingly generate RDMs. Step 6) and its sub-steps implement the CA-CFAR.

In Step 6), P_{F} is the expected false-alarm rate; N_{g}^k and N_{g}^l denote the number of gap samples on each side of the grid under test (GUT) along the k- and l-dimensions; likewise, N_{r}^k and N_{r}^l denote the number of reference samples. The gap samples will be excluded while the reference samples will be used, when estimating the power of local IN background. Given a Gaussian IN background, the maximum likelihood estimate of the power is the mean of the signal power of the selected reference grids, i.e.,

$$\hat{\sigma}_{k^*,l^*}^2 = \frac{1}{|\Omega_{k^*,l^*}^{\mathrm{r}}|} \sum_{(k,l) \in \Omega_{k^*,l^*}^{\mathrm{r}}} |V_k^{\mathsf{X}}[l]|^2, \ \mathsf{X} \in \{\mathrm{r}, \mathrm{c}\},$$
$$\Omega_{k^*,l^*}^{\mathrm{r}} = \left\{ (k,l) \middle| \begin{smallmatrix} k = k^* - N_{\mathrm{r}}^k - N_{\mathrm{g}}^k, \cdots, k^* + N_{\mathrm{r}}^k + N_{\mathrm{g}}^k; \\ l = l^* - N_{\mathrm{r}}^l - N_{\mathrm{g}}^l, \cdots, l^* + N_{\mathrm{r}}^l + N_{\mathrm{g}}^l \end{smallmatrix} \right\} \setminus \left\{ (k,l) \middle| \begin{smallmatrix} k = k^* - N_{\mathrm{g}}^k, \cdots, k^* + N_{\mathrm{g}}^k; \\ l = l^* - N_{\mathrm{g}}^l, \cdots, l^* + N_{\mathrm{g}}^l \end{smallmatrix} \right\}, \tag{17}$$

where (k^*, l^*) denotes the index of GUT, $\Omega_{k^*,l^*}^{\mathrm{r}}$ denotes the index set of reference grids, $\{\}\backslash\{\}$ gives the set difference, and $|\Omega|$ denotes the number of entries in the set Ω. Using $\hat{\sigma}_{k^*,l^*}^2$, we can set the CA-CFAR threshold as [33, (16.23)],

$$\mathsf{T} = \beta \hat{\sigma}_{k^*,l^*}^2, \ \beta = |\Omega_{k^*,l^*}^{\mathrm{r}}| \left(\mathsf{P}_{\mathrm{F}}^{-1/|\Omega_{k^*,l^*}^{\mathrm{r}}|} - 1 \right). \tag{18}$$

If $|V^{\mathsf{X}}_{k^*}[l^*]|^2 \geq \mathsf{T}$, we report the presence of a target at (k^*, l^*). The coarse estimates of the delay and Doppler frequency of the target, say the p-th, can be obtained as

$$\hat{\tau}_p = l^* T_{\mathrm{s}};\ \hat{\nu}_p = k^* \Big/ \left((\tilde{M} - \bar{Q})\tilde{N} T_{\mathrm{s}}\right), \tag{19}$$

where the relationship among relevant variables, as given in (6) and (14), is used for the above result. For applications requiring high-accuracy estimations of target location and velocity, various methods for parameter refinement are available in the literature, such as the conventional multiple signal clarification (MUSIC) [35] and a much newer DFT-interpolation-based estimator [36] etc. In a parallel work [37], we have specifically studied the OTFS-based ISAC with a low-complexity target estimator developed. Interested readers are referred to [37] form more details on target estimation.

Before ending the section, the last note is given on the computational complexity of the proposed sensing framework. From Table II, we see that the explicit complexity is dominated by the computations performed in Steps 3)-6). An implicit complexity, however, lies in the computation of $S_n[m]$ which is an extra compared with previous designs, e.g., COS [10] and C-COS [11]. Since $S_n[m]$ is the result of $\tilde{N}$ numbers of $\tilde{M}$-point DFTs, computing it incurs the complexity of $\mathcal{O}\{\tilde{N}\tilde{M}\log\tilde{M}\}$, where $\mathcal{O}\{\tilde{M}\log\tilde{M}\}$ is complexity of the $\tilde{M}$-point DFT (under the fast implementation [38]). Step 3) shares the same complexity of $\mathcal{O}\{\tilde{N}\tilde{M}\log\tilde{M}\}$. The complexity of generating an RDM, performing either Step 4) or Step 5), is dominated by the two-dimensional DFT and can be given by $\mathcal{O}\{\tilde{N}\tilde{M}\log\tilde{M}+\tilde{M}\tilde{N}\log\tilde{N}\}$. Step 6) essentially processes the RDM by a two-dimensional filter, and hence can be performed through the same two-dimensional Fourier transform as in Steps 4) and 5) [39]. Consequently, we can say that the overall computational complexity of the proposed sensing framework is $\mathcal{O}\{\tilde{N}\tilde{M}\log\tilde{M} + \tilde{M}\tilde{N}\log\tilde{N}\}$.

IV. Performance Analysis

In this section, we analyze the interference and noise background in the two RDMs obtained in (15) and (16). Then we derive, analyze and compare their SINRs, through which the question in Section II-C3 will be answered. Moreover, insights into the parameter design for the proposed sensing framework will also be drawn.

A. Preliminary Results

From (15) and (16), we see that both RDMs are obtained based on $X_n[m]$ given in (14). Thus, we analyze first its three signal components, i.e., $S_n[m]$, $Z_n[m]$ and $W_n[m]$. Their useful features are provided here. In particular, their distributions are provided in Lemma 1 with the proof given in Appendix A. The independence of $S_n[m]$, $Z_n[m]$ and $W_n[m]$ over n is given in Lemma 2; see Appendix B for the proof. In addition, the independence of the signals over m is illustrated in Lemma 3; see Appendix C for the proof.

Lemma 1: *The useful signal and the noise in (14) satisfy*

$$\begin{aligned} S_n[m] &\sim \mathcal{CN}(0, \sigma_d^2); \\ W_n[m] &\sim \mathcal{CN}\left(0, \sigma_W^2\right),\ \sigma_W^2 = \left(1 + \tilde{Q}/\tilde{M}\right)\sigma_w^2, \end{aligned} \tag{20}$$

where σ_d^2 is the power of communication data symbols, i.e., d_i given in (1), and σ_w^2 is power of the receiver noise, i.e., $w[i]$ given in (6). Moreover, provided that $\alpha_0, \alpha_1, \cdots, \alpha_{P-1}$ are uncorrelated, the interference term in (14) conforms to

$$Z_n[m] \sim \mathcal{CN}\left(0, \sigma_Z^2\right),\ \sigma_Z^2 = \frac{\tilde{Q}\sigma_d^2\sigma_P^2}{\tilde{M}},\ \sigma_P^2 = \sum_{p=0}^{P-1}\sigma_p^2, \tag{21}$$

where σ_p^2 is the power of the p-th scattering coefficient, i.e., α_p given in (6).

Lemma 2: *Given $\tilde{M} > (\tilde{Q} + \bar{Q})$ and at any m, $Z_n[m]$ is i.i.d. over n, whereas $S_n[m]$ and $W_n[m]$ are each independent over either the set of odd n's or that of even n's. In addition, we have, at any m,*

$$\begin{aligned} \mathbb{C}\left(S_n[m], S_{n+1}[m]\right) &= \bar{Q}/\tilde{M}; \\ \mathbb{C}\left(W_n[m], W_{n+1}[m]\right) &= (\tilde{Q} + \bar{Q})/\tilde{M}. \end{aligned} \tag{22}$$

where $n = 0, 1, \cdots, \tilde{N} - 2$ and $\mathbb{C}(x, y) = \frac{|\mathbb{E}\{xy^*\}|}{\sqrt{\mathbb{E}\{|x|^2\}\mathbb{E}\{|y|^2\}}}$ is the absolute correlation coefficient between x and y.

Lemma 3: *For any n, $S_n[m]$ and $W_n[m]$ are independent over m, while $Z_n[m]$ is not and satisfies*

$$\mathbb{C}\left(Z_n[m_1], Z_n[m_2]\right) = \frac{\sin\left(\frac{2\pi}{\tilde{M}}\frac{\tilde{Q}(m_1 - m_2)}{2}\right)}{\tilde{Q}\sin\left(\frac{2\pi}{\tilde{M}}\frac{(m_1 - m_2)}{2}\right)}. \tag{23}$$

From (15) and (16), we notice that the SINR improvement is maximized when the IN background is independent over the range-Doppler grids, also known as 'white'. However, we see from Lemmas 2 and 3, the interference and noise signals are somewhat dependent over range-Doppler grids. More interestingly, there is a trade off in this regard caused by $\frac{\tilde{Q}}{\tilde{M}}$. To reduce the correlation of $S_n[m]$ and $W_n[m]$ along n, we prefer $\tilde{M} \gg (\tilde{Q}+\bar{Q})$ which also means $\tilde{M} \gg \tilde{Q}$. However, according to (23), reducing $\frac{\tilde{Q}}{\tilde{M}}$ will heavily increase the correlation of $Z_n[m]$ over m. In an extreme case, consider $\tilde{Q}$ takes one, the smallest value. We then have $\mathbb{C}\left(Z_n[m_1], Z_n[m_2]\right) = 1\ (\forall m_1, m_2)$. As will be shown shortly, the dependence of $S_n[m]$, $W_n[m]$ and $Z_n[m]$ over n and m makes it difficult to analyze the distribution of the IN background in the RDMs. This, nevertheless, will be conquered.

B. Analyzing Signal Components in Two RDMs

We start with analyzing the distribution of the IN background, i.e., $W_k^{\mathrm{r}}[l] + Z_k^{\mathrm{r}}[l]$, in the ratio-based RDM. According to (15), $W_k^{\mathrm{r}}[l] + Z_k^{\mathrm{r}}[l]$ can be rewritten as

$$Z_k^{\mathrm{r}}[l] + W_k^{\mathrm{r}}[l] = \sum_{n=0}^{\tilde{N}-1}\sum_{m=0}^{\tilde{M}-1}\frac{\overbrace{\left(Z_n[m] + W_n[m]\right)\mathcal{Z}_{\tilde{M}}^{-ml}\mathcal{Z}_{\tilde{N}}^{nk}}^{D_{n,m}^{k,l}}}{S_n[m]}. \tag{24}$$

Since $Z_n[m]$ and $W_n[m]$ are independent Gaussian variables, their sum is also Gaussian distributed. Moreover, given

$\forall k,m,n,l$, $\mathcal{Z}_{\tilde{M}}^{-lm}$ and $\mathcal{Z}_{\tilde{N}}^{nk}$ have deterministic values, as defined in (3). Accordingly, applying Lemma 1, we obtain

$$D_{n,m}^{k,l} \sim \mathcal{CN}\left(0, (\sigma_Z^2+\sigma_W^2)/\tilde{M}\tilde{N}\right), \tag{25}$$

where the coefficient of the variance is from the two DFT bases; see (3). Then, the summand in (24) becomes the ratio of two uncorrelated complex Gaussian variables. Such a ratio conforms to a Cauchy distribution [40]. Now that $Z_k^{\mathrm{r}}[l]+W_k^{\mathrm{r}}[l]$ becomes the sum of Cauchy variables, one would think of using the central limit theorem (CLT) to approximate the summation as a Gaussian distribution. Unfortunately, CLT is not applicable to Cauchy variables, as they have infinite variances [40]. To this end, we provide a remedy below, in light of the fact that the CLT is applicable to the truncated Cauchy distributions [41].

Instead of using $S_n[m]$ as divisor directly, we can use $\mathsf{g}S_n[m]$, where g a real positive coefficient. Since $\mathsf{g}S_n[m] \sim \mathcal{CN}\left(0, \mathsf{g}^2\sigma_d^2\right)$ according to Lemma 1, we can take a sufficiently large g such that the probability of the event $|\mathsf{g}S_n[m]|<1$ can be reduced to a small value, say ϵ. Moreover, if $\epsilon I<1$, then out of I samples of $\mathcal{CN}\left(0,\mathsf{g}^2\sigma_d^2\right)$, the event $|\mathsf{g}S_n[m]|<1$ may not happen at all. According to [37, Lemma 3], the critical value of g, leading to $\epsilon = 1/I$, can be given by

$$\mathsf{g}_{\mathrm{c}} = 1\Big/\left(\sigma_d\sqrt{\ln\frac{I-1}{I}}\right). \tag{26}$$

Based on the above illustration, we can revise the ratio-based RDM as follows,

$$\begin{aligned}
\tilde{V}_k^{\mathrm{r}}[l] &= \sum_{n=0}^{N-1}\sum_{m=0}^{M-1}\mathbb{I}_{\mathcal{E}}\left\{\frac{X_n[m]}{\mathsf{g}S_n[m]}\right\}\mathcal{Z}_M^{-ml}\mathcal{Z}_N^{nk}\\
&\approx \sum_{p=0}^{P-1}\frac{\tilde{\alpha}_p}{\mathsf{g}}\mathcal{S}_{\bar{M}}\left(l-\mathsf{l}_p\right)\mathcal{S}_{\tilde{N}}\left(\mathsf{k}_p-k\right)+\tilde{W}_k^{\mathrm{r}}[l]+\tilde{Z}_k^{\mathrm{r}}[l],\\
\text{s.t. } \tilde{\mathsf{X}}_k^{\mathrm{r}}[l] &= \sum_{n=0}^{N-1}\sum_{m=0}^{M-1}\mathbb{I}_{\mathcal{E}}\left\{\frac{\mathsf{X}_n[m]}{\mathsf{g}S_n[m]}\right\}\mathcal{Z}_M^{-ml}\mathcal{Z}_N^{nk}, \mathsf{X}\in\{W,Z\}\\
&\quad \mathbb{I}_{\mathcal{E}}\{\cdot\}=1 \text{ if event } \mathcal{E} \text{ happens; otherwise } \mathbb{I}_{\mathcal{E}}\{\cdot\}=0,\\
&\quad \mathcal{E}\triangleq\{|\mathsf{g}S_n[m]|\geq 1\},
\end{aligned} \tag{27}$$

where $X_n[m]$ is given in (14) and $\mathsf{g}S_n[m]$ is used as the divisor compared with using $S_n[m]$ in (15). Note that the approximation is based on that $\mathbb{I}_{\mathcal{E}}=0$ can barely happen with a sufficiently large g. For the same reason, we will drop the operator $\mathbb{I}_{\mathcal{E}}\{\cdot\}$ below for notation simplicity. But bear in mind that $\mathbb{I}_{\mathcal{E}}\{\cdot\}$ shall still be applied.

Now we are able to invoke the CLT based on (27). However, there is one more trap — the summands under the CLT need to be i.i.d., while, as indicated by Lemmas 2 and 3, the i.i.d. condition is not satisfied here. To this end, we resort to the case $\tilde{M}\gg(\tilde{Q}+\bar{Q})$, under which the correlation of $S_n[m]$ and $W_n[m]$ over n can be negligibly weak. As illustrated at the end of Section IV-A, $\tilde{M}\gg(\tilde{Q}+\bar{Q})$ can severely increase the correlation of $Z_n[m]$ over m. Nevertheless, we discover that applying the CLT along the n-dimension first can approximately remove the correlation of the resulted Gaussian distributions over m. More details are given in Appendix D, while the results are summarized in the following proposition.

Proposition 1: *Provided that $\tilde{N}$ is large and $\tilde{M}\gg(\tilde{Q}+\bar{Q})$, the IN background of the ratio-based RDM obtained in (27) approaches a complex centered Gaussian distribution which satisfies*

$$\begin{aligned}
\tilde{W}_k^{\mathrm{r}}[l]+\tilde{Z}_k^{\mathrm{r}}[l] &\sim \mathcal{CN}\left(0, \frac{(\sigma_Z^2+\sigma_W^2)\mathsf{b}(\epsilon)}{\mathsf{g}^2\sigma_d^2}\right),\\
\text{s.t. } \mathsf{b}(\epsilon) &= 2\ln\left(2(1-\epsilon)\Big/\left(\mathsf{e}\sqrt{\epsilon(2-\epsilon)}\right)\right),
\end{aligned} \tag{28}$$

where σ_Z^2 and σ_W^2 are given in Lemma 1, ϵ is a sufficiently small number and e denotes the base of the natural logarithm.

Despite the complex expression of the variance in (28), it actually has a clear structure. Specifically, the fraction $\frac{(\sigma_Z^2+\sigma_W^2)}{\mathsf{g}^2\sigma_d^2}$ is the ratio between the variance of $D_{n,m}^{k,l}$ and that of $\mathsf{g}S_n[m]$; in parallel with that $\tilde{W}_k^{\mathrm{r}}[l]+\tilde{Z}_k^{\mathrm{r}}[l]$ is the ratio between the two random variables. Such a ratio is known to have a heavy-tail PDF [40] and hence the coefficient $\mathsf{b}(\epsilon)$, greater than one in general, acts like a penalty factor to account for the heavy tail. Next, we elaborate more on $\mathsf{b}(\epsilon)$. According to [37, Appendix D], ϵ is the probability that $\left|\Re\{\tilde{W}_k^{\mathrm{r}}[l]+\tilde{Z}_k^{\mathrm{r}}[l]\}\right|$ is larger than a threshold, where $\Re\{\}$ takes the real part of a complex number. Regardless of the specific expression of the threshold, we hope ϵ is such a small probability that out of $\tilde{M}\tilde{N}$ samples of $\tilde{W}_k^{\mathrm{r}}[l]+\tilde{Z}_k^{\mathrm{r}}[l]$, less than one sample can have the magnitude of its real part exceed the threshold. So a critical value of ϵ is $1/\left(\tilde{M}\tilde{N}\right)$. Substituting the value into (28) leads to

$$\mathsf{b}_{\mathrm{c}} = \mathsf{b}\left(1/\left(\tilde{M}\tilde{N}\right)\right) = 2\left(\ln\left(\frac{2(\tilde{M}\tilde{N}-1)}{\sqrt{2\tilde{M}\tilde{N}-1}}\right)-1\right). \tag{29}$$

Note that $\tilde{M}\tilde{N}\approx I$, the number of samples in the whole block can be tens of thousands and even greater.

With reference to the analysis yielding Proposition 1, we can similarly analyze the distributions of the signal components in the CCC-based RDM obtained in (16). This time, the CLT is directly applicable to the summands in (16), as each is a product of two Gaussian variables and has a limited variance [42]. However, the useful signal in the CCC-based RDM is substantially different from that in the ratio-based RDM; see (16) and (27). Thus, we provide some more analysis in Appendix E, with the focus on the useful signal in the CCC-based RDM. The following proposition summarizes the analytical results.

Proposition 2: *Provided large $\tilde{M}$ and $\tilde{N}$ as well as $\tilde{M}\gg(\tilde{Q}+\bar{Q})$, the signal components of the RDM obtained in (16) approach Gaussian distributions that approximately satisfy*

$$S_k^{\mathrm{c}}[l] \sim \begin{cases} \mathcal{N}\left(\sigma_d^2\sqrt{\tilde{M}\tilde{N}}, \sigma_d^4\right) & l=\mathsf{l}_p \text{ and } k=\mathsf{k}_p \\ \mathcal{N}\left(0,\sigma_d^4\right) & l\neq\mathsf{l}_p \text{ or } k\neq\mathsf{k}_p \end{cases}; \tag{30}$$

$$W_k^{\mathrm{c}}[l]+Z_k^{\mathrm{c}}[l] \sim \mathcal{CN}\Big(0,\sigma_d^2(\sigma_Z^2+\sigma_W^2)\Big). \tag{31}$$

Detecting in Gaussian IN background has been widely studied for decades. Thus, Propositions 1 and 2 allow us to

employ many existing detectors to detect targets from the RDMs obtained under the proposed sensing framework. The CA-CFAR has been briefly reviewed in Section III. The two propositions also allow us to analyze and compare the SINRs in the two RDMs and draw insights into sensing parameter design. This is carried out next.

C. Comparison and Insights

The SINRs in the two RDMs are first derived based on Propositions 1 and 2. Based on (27), the power of the useful signal in the ratio-based RDM can be given by $\sigma_P^2\tilde{M}\tilde{N}/\mathsf{g}^2$, where $\sigma_P^2=\sum_{p=0}^{P-1}\sigma_p^2$. Then, combining the power of the IN terms derived in Proposition 1, we obtain the SINR of the ratio-based RDM, as given by

$$\gamma_V^{\mathrm{r}}=\frac{\tilde{M}\tilde{N}\sigma_P^2\sigma_d^2}{(\sigma_Z^2+\sigma_W^2)\mathsf{b}(\epsilon)}=\frac{\tilde{M}\tilde{N}}{\left(\frac{\tilde{Q}}{M}+\left(1+\frac{\tilde{Q}}{M}\right)\frac{1}{\gamma_0\sigma_P^2}\right)\mathsf{b}(\epsilon)},$$
$$\text{s.t. } \gamma_0=\sigma_d^2\Big/\sigma_w^2,\ \sigma_P^2=\sum_{p=0}^{P-1}\sigma_p^2, \tag{32}$$

where the expressions of σ_Z^2 and σ_W^2 given in Lemma 1 are used to get the final result. The above SINR can be simplified under certain asymptotic conditions. In particular, we have

$$\gamma_V^{\mathrm{r}}\begin{cases}\overset{\gamma_0\ll\frac{1}{\sigma_P^2}}{\approx}\ \frac{\tilde{M}\left(\frac{(I-\bar{Q}-\bar{Q})}{(\tilde{M}-\bar{Q})}\right)\gamma_0\sigma_P^2}{\left(1+\frac{\tilde{Q}}{M}\right)\mathsf{b}(\epsilon)}\overset{(a)}{\approx}\frac{I\gamma_0\sigma_P^2}{\left(1-\frac{\bar{Q}}{M}\right)\left(1+\frac{\tilde{Q}}{M}\right)\mathsf{b}(\epsilon)};\\ \overset{\gamma_0\gg\frac{1}{\sigma_P^2}}{\approx}\ I\Big/\left(\left(1-\frac{\bar{Q}}{M}\right)\frac{\tilde{Q}}{M}\mathsf{b}(\epsilon)\right)\end{cases} \tag{33}$$

where $\overset{\gamma_0\ll\frac{1}{\sigma_P^2}}{\approx}$ is obtained by (I) suppressing $\frac{\tilde{Q}}{M}$ from the denominator of (32) as $\gamma_0\ll\frac{1}{\sigma_P^2}$ leads to $\frac{\tilde{Q}}{M}\ll\left(1+\frac{\tilde{Q}}{M}\right)\frac{1}{\gamma_0\sigma_P^2}$; and (II) replacing $\tilde{N}$ with its expression given in (11) while suppressing the flooring operator. Moreover, $\overset{(a)}{\approx}$ is due to $I=(M+Q)N\gg(\bar{Q}+\tilde{Q})$. The second line in (33) can be obtained similarly.

For the CCC-based RDM, its SINR can be obtained by applying Proposition 2 in (16). In particular, we have

$$\gamma_V^{\mathrm{c}}=\frac{(\tilde{M}\tilde{N}+1)\sigma_P^2\sigma_d^4}{(\sigma_Z^2+\sigma_W^2)\sigma_d^2+\sigma_P^2\sigma_d^4}=\frac{(\tilde{M}\tilde{N}+1)}{\frac{\tilde{Q}}{M}+\left(1+\frac{\tilde{Q}}{M}\right)\frac{1}{\gamma_0\sigma_P^2}+1}, \tag{34}$$

where $\sigma_P^2\sigma_d^4$ in the denominator of the middle result is the interference caused by $S_k^{\mathrm{c}}[l]$ at $l\neq\mathsf{l}_p$ or $k\neq\mathsf{k}_p$. With reference to the way (33) is obtained, we can also attain the asymptotic γ_V^{c}, as given by

$$\gamma_V^{\mathrm{c}}\begin{cases}\overset{\gamma_0\ll\frac{1}{\sigma_P^2}}{\approx}\ I\gamma_0\sigma_P^2\Big/\left(\left(1-\frac{\bar{Q}}{M}\right)\left(1+\frac{\tilde{Q}}{M}\right)\right)\\ \overset{\gamma_0\gg\frac{1}{\sigma_P^2}}{\approx}\ I\Big/\left(\left(1-\frac{\bar{Q}}{M}\right)\left(1+\frac{\tilde{Q}}{M}\right)\right)\end{cases}. \tag{35}$$

The SINRs derived in (32) and (34) can be adapted for the RDMs obtained in the framework of COS, i.e., (8) and (10). As reviewed in Section II-B, COS complies with the underlying communication system. Thus, we can take $\tilde{M}=M$ and $\tilde{N}=N$ in (32) and (34). Moreover, since COS uses the original communication CP, σ_Z^2 in (32) and (34), which is the power of the interference caused by the proposed VCP, can be suppressed, and σ_W^2 can be replaced by σ_w^2. Under the above changes, the SINRs of the RDMs in (8) and (10) can be, respectively, given by

$$\gamma_U^{\mathrm{r}}=\frac{MN\gamma_0\sigma_P^2}{\mathsf{b}(\epsilon)}\overset{(a)}{=}\frac{I\gamma_0\sigma_P^2}{\left(1+\frac{Q}{M}\right)\mathsf{b}(\epsilon)}\ (\forall\gamma_0);$$
$$\gamma_U^{\mathrm{c}}=\frac{(MN+1)\gamma_0\sigma_P^2}{1+\gamma_0\sigma_P^2}\begin{cases}\overset{\gamma_0\ll\frac{1}{\sigma_P^2}}{\approx}\ I\gamma_0\sigma_P^2\Big/\left(1+\frac{Q}{M}\right)\\ \overset{\gamma_0\gg\frac{1}{\sigma_P^2}}{\approx}\ I\Big/\left(1+\frac{Q}{M}\right)\end{cases} \tag{36}$$

where $\overset{(a)}{=}$ is obtained by replacing N with $\frac{I}{(M+Q)}$, the same replacement is also performed for γ_U^{c}, and the approximations are similarly attained, as done in (33). Now, we are ready to make some comparisons using the SINR expressions.

Remark 3: For the ratio-based RDM, we make the following comparisons between COS and the proposed sensing:

3a) In low SNR regions, such that $\gamma_0=\frac{\sigma_d^2}{\sigma_w^2}\ll\frac{1}{\sigma_P^2}$, the proposed sensing framework has a greater SINR than COS with a gain no less than $\frac{1}{1-\frac{\bar{Q}}{M}}$, provided $\frac{\tilde{Q}}{M}\leq\frac{Q}{M}$;

3b) Provided the maximum round-trip delay of a target is smaller than the communication CP duration, i.e., $\max_{\forall p}\{\tau_p\}\leq QT_{\mathrm{s}}$, COS can have a greater SINR than the proposed sensing framework for $\gamma_0>\frac{1+\frac{Q}{M}}{\left(1-\frac{\bar{Q}}{M}\right)\frac{\tilde{Q}}{M}\sigma_P^2}$;

3c) Provided $\max_{\forall p}\{\tau_p\}>QT_{\mathrm{s}}$, the result in Remark 3b) may not hold any more; moreover, the proposed sensing framework can have a greater SINR than COS;

The first two results can be readily attained based on (33) and (36). It is noteworthy that the condition $\max_{\forall p}\{\tau_p\}\leq QT_{\mathrm{s}}$ is implicitly required by COS to remove communication data symbols for generating RDMs; see the review in Section II-B. If the condition is unsatisfied, the SINR of COS, as given in (36), becomes invalid. However, for the fact that COS cannot effectively remove communication data symbols any more while the proposed sensing can, we attain the result in Remark 3c). As will be validated by Fig. 3 in Section V, the SINRs of the two RDMs under COS degrade severely, as $\max_{\forall p}\{\tau_p\}$ exceeds QT_{s}.

Remark 4: For the CCC-based RDM, provided $\frac{\tilde{Q}}{M}\leq\frac{Q}{M}$, the proposed sensing always has a greater SINR than COS regardless of γ_0 and the SINR gain is no less than $\frac{1}{1-\frac{\bar{Q}}{M}}$. The results can be easily validated using (35) and (36). An intriguing question is why the relationship between COS and the proposed sensing is substantially different under the two RDMs. In essence, this is caused by the different ways the communication data symbols are removed for generating the two RDMs. For the ratio-based RDM, the pointwise division, as shown in (15), magnifies the IN background by introducing the multiplicative coefficient $\mathsf{b}(\epsilon)$. In contrast, the pointwise product for the CCC-based RDM; see (16), introduces an additive interference $\sigma_P^2\sigma_d^4$; see (34). While the VCP-incurred

interference does not bother COS, the CCC-incurred interference exists in both COS and the proposed sensing framework.

Remark 5: Some comparisons between the ratio- and CCC-based RDMs are made here. Based on (33) and (35), we can attain the following results for the proposed sensing:

5a) In low SNR regions where $\gamma_0 \ll 1/\sigma_P^2$, the CCC-based RDM has an SINR that is $\mathsf{b}(\epsilon)$ times the SINR in the ratio-based RDM, where $\mathsf{b}(\epsilon) > 1$ in general; see (29).

5b) In high SNR regions where $\gamma_0 \gg 1/\sigma_P^2$, the ratio-based RDM can have a greater SINR than the CCC-based RDM, provided $\mathsf{b}(\epsilon) \leq \frac{\tilde{M}}{\bar{Q}}$.

5c) Regardless of γ_0, the CCC-based RDM always has a greater SINR than the ratio-based RDM, if $\mathsf{b}(\epsilon) > \frac{\tilde{M}}{\bar{Q}} + 1$.

Based on (36), similar results as above can be given for COS:

5d) The result in 5a) directly applies to COS;

5e) In high SNR regions where $\gamma_0 \gg 1/\sigma_P^2$, the CCC-based RDM has a greater SINR than the ratio-based RDM, if $\mathsf{b}(\epsilon) > \gamma_0 \sigma_P^2$, while if $\mathsf{b}(\epsilon) < \gamma_0 \sigma_P^2$ the ratio-based RDM has a greater SINR.

D. Criteria for Setting Key Sensing Parameters

Unlike COS that follows with the underlying communication system, our sensing framework has the flexibility of catering different sensing needs via adjusting several key parameters: $\tilde{M}$, $\tilde{Q}$ and $\bar{Q}$ ($\tilde{N}$ is determined given the former three). Below, we illustrate the criteria for setting these parameters to optimize sensing performance.

First, we can set $\tilde{Q}$ based on the required maximum sensing distance, as denoted by $r_{\max}$. From Section III, the sensing distance of the proposed design is given by $\frac{\mathsf{C}\tilde{Q}T_{\mathrm{s}}}{2}$, which, equating with $r_{\max}$, yields

$$\tilde{Q} = 2r_{\max}/\mathsf{C}T_{\mathrm{s}}. \tag{37}$$

It is worth noting that the issue of CP-limited sensing, as described in Section II-C1, is addressed by introducing $\tilde{Q}$. Unlike in COS and its variants where $r_{\max}$ is determined by Q, we now can set $\tilde{Q}$ to satisfy $r_{\max}$ (provided a sufficient link budget).

Second, we determine $\tilde{M}$ given the requirements on velocity measurement. Applying the analysis in Section II-C2, the maximum measurable value and the resolution of Doppler frequency of the proposed sensing framework are given by

$$\nu_{\max} = 1\Big/\big(2(\tilde{M}-\bar{Q})T_{\mathrm{s}}\big);\ \Delta_\nu \approx 1\Big/\big(IT_{\mathrm{s}}\big). \tag{38}$$

Thus, to cater the expected $\nu_{\max}^*$ we need to keep $\tilde{M} \leq 1\Big/\big(2\nu_{\max}^* T_{\mathrm{s}}\big) + \bar{Q}$. Moreover, we prefer to have a relatively large[2] $\tilde{M}$ which can lead to a small $\frac{\bar{Q}}{\tilde{M}}$ and hence a high SINR in both RDMs; see (33) and (35). It is noteworthy that the issue of limited velocity measurement, as illustrated in Section II-C2, is now addressed by introducing $\tilde{M}$ and $\bar{Q}$. Instead of having an M-limited $\nu_{\max}$, we now have the flexibility of configuring $\tilde{M}$ to satisfy the requirement on $\nu_{\max}$.

[2]Note that, if $\bar{Q}/\tilde{M}$ is fixed, the larger $\tilde{M}$ the smaller $\tilde{N}(\approx I/(\tilde{M}(1-\bar{Q}/\tilde{M})))$ will become. This may affect the precision of results given in Propositions 1 and 2 which expect both $\tilde{M}$ and $\tilde{N}$.

TABLE III: Simulation Parameters

Var.	Description	IEEE 802.11ad
f_{c}	Carrier frequency	60.48 GHz
B	Bandwidth	1.825 GHz
M	No. of sub-carriers per symbol	512
Q	CP length	128
N	No. of symbols	143 (0.05 ms packet)
I	Total No. of samples; see (4)	$N(M+Q) = 91520$
σ_d^2	Power of data symbol d_i; see (1)	0 dB
σ_p^2	Power of α_p; see (6)	$[0, -10, -20]$ dB
r_p	Target range	$\mathcal{U}_{[0,10]\ \mathrm{m}}$ †
v_p	Target velocity	$\mathcal{U}_{[-139,139]\ \mathrm{m/s}}$
σ_w^2	Variance of AWGN $w[i]$; see (6)	-20 dB

† $\mathcal{U}_{[x,y]}$ denotes a uniform distribution in the region give by the subscript.

Third, given $\tilde{M}$, we can then set $\bar{Q}$. To increase the SINR in both RDMs, we expect to have $\bar{Q}$ as large as possible; see (33) and (35). However, the larger $\bar{Q}$ the more correlated the signals between adjacent sub-blocks can be; see Lemmas 2 and 3. As seen from Propositions 1 and 2, the correlation can make the results less precise. The detailed impact, however, is difficult to analyze. As will be shown through the simulations in Figs. 4 and 5, the derivations and analysis in Sections IV-B and IV-C are consistently precise when $\bar{Q}$ takes from a small value to the one as large as $\tilde{M}/2 - \tilde{Q}$.

V. Simulation Results

Simulations are performed in this section to validate the proposed design. The simulation parameters are set with reference to [11] and are summarized in Table III. The root raised cosine (RRC) filter with the roll-off coefficient of 0.2 is used at both the communication transmitter and the sensing receiver. In generating target echo signals, a four-times upsampling is performed by the transmitter RRC filter; the target delay and Doppler frequency are added at the high sampling rate; and a four-times decimating is performed at the receiver RRC filter. This generates off-grid range and Doppler values, making the simulations comply with practical scenarios. Further, the Swerling 0 target model [33, Table 7-3] is employed in the simulation. Namely, $\alpha_p = \sqrt{\sigma_p^2}$ is taken over independent trials. However, to have independent scattering coefficients, the phase of α_p $(\forall p)$ is uniformly drawn from $[0, 2\pi]$, yet independently over targets and trials.

The benchmark sensing framework is COS [10], as reviewed in Section II-B. The original COS, as developed for OFDM [10], uses the ratio-based RDM given in (8), while the variant of COS, as developed for DFT-S-OFDM [11], employs the CCC-based RDM given in (10). As illustrated in Remark 1, for both OFDM and DFT-S-OFDM, the time-domain transmitted communication signals conform to Gaussian distributions, which is similar to OTFS. Therefore, for fair comparison, we unitedly use OTFS modulation for all methods to be simulated. In essence, it is the way a block of echo signal is segmented, rather than the communication waveforms, that differentiates COS and the proposed sensing framework. Substantially differentiating our sensing framework from the existing ones of the same kind, e.g., [10] and [11], is mainly the way how the RDMs are generated. Therefore, following the most related previous works [10] and [11], the SINRs of the RDMs and the

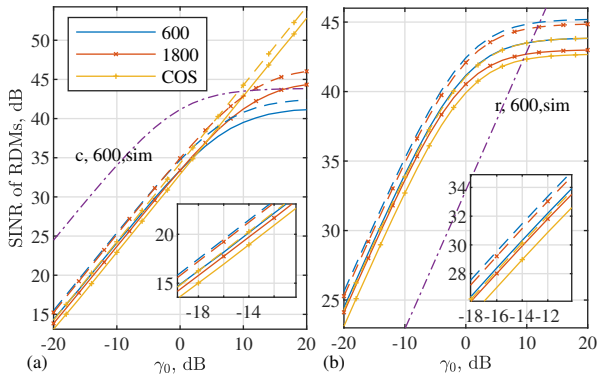

Fig. 2: SINRs in the RDMs versus γ_0 defined in (32), where three targets are set as specified in Table III. The ratio-based RDMs are shown in Fig. 2(a), while the CCC-based RDMs in Fig. 2(b). The two sub-figures share the same legend, where the numbers are the values of $\tilde{M}$ used for the proposed design. Corresponding to the solid curves, the dash ones are the theoretical SINRs derived in (32), (34) and (36). For comparison convenience, the curve 'c, 600, sim' in Fig. 2(a) is copied from Fig. 2(b) and the curve 'r, 600, sim' in Fig. 2(b) is from Fig. 2(a).

target detection performance that is directly related to SINRs, are employed as the main performance metrics in the following simulations.

In the legends of the simulation results, we use 'r' to indicate the 'ratio-based RDM', 'c' the 'CCC-based RDM', 'sim' the simulated result and 'pp' the 'proposed design'.

A. Illustrating SINRs in RDMs

Fig. 2 plots the SINRs of the ratio- and CCC-based RDMs versus γ_0, under different values of $\tilde{M}$. In this simulation, $\tilde{Q} = Q$, $\bar{Q} = 150$ and other parameters are given in Table III. Overall, we see that the derived SINRs can precisely describe the actual (simulated) SINRs. This validates the analysis in Section IV-B. More specifically, we see from Fig. 2(a) that the proposed design achieves higher SINRs in the ratio-based RDM than COS in the case of $\gamma_0 \ll 1$, which validates Remark 3a). We also see Fig. 2(a) that as $\tilde{M}$ increases the gap between the proposed design and COS becomes smaller for $\gamma \ll 1$. This is consistent with the SINR expression derived in (32). We further see that, when $\gamma_0 \gg 1$, COS can outperform the proposed design, which complies with Remark 3b). We see from Fig. 2(b) that the SINR achieved in the CCC-based RDM first increases with γ_0 and then converges for large γ_0's. This is consistent with (34). Moreover, we see that, for the CCC-based RDM, the proposed design achieves the higher SINR across the whole region of γ_0 compared with COS. This aligns with Remark 4. The comparison between the ratio- and CCC-based RDMs validates the analysis given in Remark 5.

It is noteworthy that the value of $\tilde{M}$ determines the maximum measurable Doppler frequency of the proposed sensing framework, as specified in (38). Approximately, the maximum Doppler frequency under $\tilde{M} = 600$ is the triple of that under $\tilde{M} = 1800$. Fig. 2 shows that the proposed design achieves consistent SINRs under the two substantially different cases. This manifests the flexibility of the proposed sensing framework in adapting to different requirements on Doppler

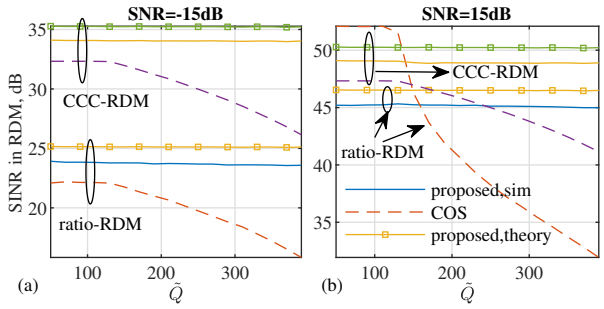

Fig. 3: SINRs in RDMs versus $\tilde{Q}$ (the length of VCP), where the values of $\tilde{M}$ and $\bar{Q}$ are changed with $\tilde{Q}$ to keep $\frac{\tilde{Q}}{\tilde{M}} = \frac{1}{4}$ and $\frac{\bar{Q}}{\tilde{M}} = \frac{1}{3}$. A single target is simulated with its distance set as $\frac{(\tilde{Q}-1)\mathsf{C}}{2B}$ m, while other parameters are set as in Table III.

measurement. Such flexibility is not owned by any existing designs of the similar kind, e.g., COS [10] and C-COS [11].

Fig. 3 illustrates the SINRs achieved by the proposed sensing framework in the two types of RDMs under different values of $\tilde{Q}$. The figure is dedicated to demonstrating the ability of the proposed sensing framework in extending the maximum sensing distance (a function of $\tilde{Q}$ given in (37)). Since the ability is independent of the number of targets, we only consider a single target in this simulation. As said in the caption of the figure, we keep the ratios $\frac{\tilde{Q}}{\tilde{M}}$ and $\frac{\bar{Q}}{\tilde{M}}$ fixed under different $\tilde{Q}$'s. Then, according to (32) and (34), we know that the SINRs achieved by the proposed design should be the same over $\tilde{Q}$, which is clearly validated by Fig. 3. This illustrates the great flexibility of proposed design in extending or reducing sensing distance as per practical sensing needs. In contrast, COS degrades severely when $\tilde{Q}$ exceeds $Q = 128$. This is because COS strictly follows the underlying communication system and cannot sense well when the echo delay is larger than the CP length; see (7).

In Fig. 3, the gap between the theoretical and simulated results is less than 2 dB and caused by the approximation used in deriving the theoretical SINR. In particular, the theoretical gain of the signal power is taken as $\tilde{M}\tilde{N}$ in Section IV-B, which, according to (14) and (15), is only accurate when l_p $(\forall p)$ and k_p $(\forall p)$ are integers. As mentioned at the beginning of Section V, we employ an upsampling and downsampling method to generate off-grid range and Doppler values, resulting in the gap seen in Fig. 3.

Figs. 4 and 5 demonstrate another great flexibility of the proposed sensing framework by showing the SINRs achieved in the two types of RDMs under different values of $\bar{Q}$. Note that three targets are set as detailed in Table III. Overall, we see from the two figures that SINRs increase with $\bar{Q}$ but the slopes decrease as $\tilde{M}$ becomes larger. This can be well seen from the analytical SINR expressions derived in (32) and (34). Moreover, we see from Fig. 4 that the SINR performance under low and high SNRs are different, while such phenomenon is not seen in Fig. 5. The rationale for this result can be seen from Remark 4. It is worth highlighting that, as seen from the figure, the analytical results match the simulated ones in the whole region of $\bar{Q}$. This manifests the high flexibility of the proposed design.

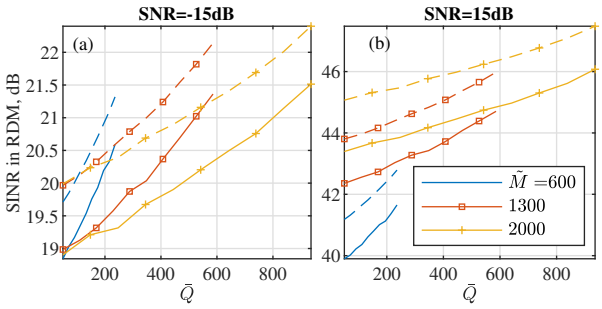

Fig. 4: SINRs in the ratio-based RDM versus $\bar{Q}$ (the number of overlapping samples between adjacent sub-blocks), where $\bar{Q} = Q$. The solid curves are simulated results while the dash ones are theoretical.

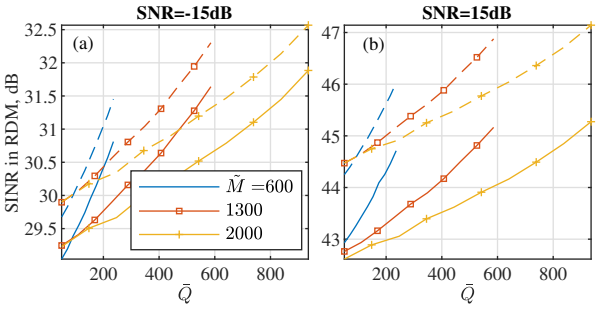

Fig. 5: SINRs in the CCC-based RDM versus $\bar{Q}$ (the number of overlapping samples between adjacent sub-blocks), where $\bar{Q} = Q$. The solid curves are simulated results while the dash ones are theoretical.

B. Illustration of Target Detection

Next, we translate the SINR results obtained above into the actual detecting performance of the proposed sensing framework. To do so, we perform the CA-CFAR according to the steps given in Table II. In the following simulations, the parameters in Step 6), Table II are set as: $N_{\rm g}^k = N_{\rm g}^l = 3$, $N_{\rm r}^k = 2$ and $N_{\rm r}^l = 5$. For a better time efficiency of simulating and calculating the detecting probability, we make two changes in the target scenario. *First*, we increase the number of targets to $P = 10$ and have their ranges linearly spaced in $[0, 10]$ m. The velocities of the targets are still uniformly distributed, as illustrated in Table III. *Second*, the powers of the targets are set as follows: $\sigma_0^2 = 0$ dB, $\sigma_p^2 = -20$ dB for $p = 1, \cdots, 4$ and $\sigma_p^2 = -30$ dB for $p = 5, \cdots, 9$. The setting of 10 targets applies to all simulation results in this section, i.e., Figs. 6-11.

Fig. 6 shows the detecting probability of COS and the proposed sensing framework under different $\tilde{M}$. Fig. 7 shows $\mathsf{P}_{\rm F}$ versus γ_0 corresponding to each curve in Fig. 6. Jointly observing the two figures, we see that the proposed sensing framework achieves better detecting performance than COS for all cases of the ratio-based RDM and most cases of the CCC-based RDM. Moreover, the improvement of the detecting probability is precisely predicted by the SINR results observed in Fig. 2. This validates our analysis and derivations provided in Section IV. From Fig. 7, we see that $\mathsf{P}_{\rm F} = 10^{-6}$ is not achieved for the CCC-based RDM under $\tilde{M} = 600$. In such a case, $\mathsf{P}_{\rm F}$ increases with γ_0. The reason is that the overlapping of consecutive sub-blocks makes the essential signal of a block partially correlated with the interference from its previous sub-block; see Fig. 1. This is validated by Fig. 8, where we can see the fake targets in the CCC-based RDM.

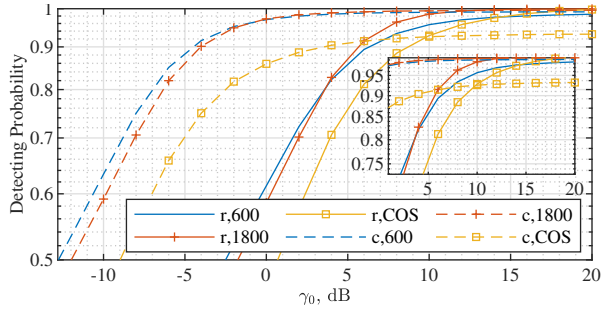

Fig. 6: Illustration of the detection performance of the proposed sensing framework, where $\bar{Q} = Q$, $\bar{Q} = 150$ and $\mathsf{P}_{\rm F} = 10^{-6}$. The numbers in the legend are the values of $\tilde{M}$.

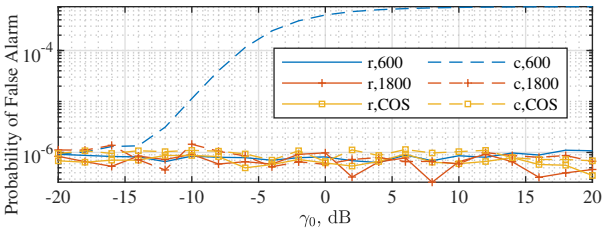

Fig. 7: Illustrating $\mathsf{P}_{\rm F}$ corresponding to the curves in Fig. 6.

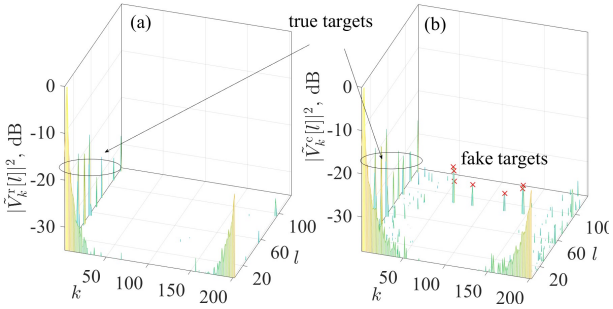

Fig. 8: Comparing the ratio- and CCC-based RDMs, as given in Figs. 8(a) and 8(b), respectively. For illustration clarity, both RDMs are noise-less and the z-axis is limited to avoid heavy interference background.

Figs. 9 and 10 illustrate the receiver operating characteristic (ROC) of the proposed sensing framework in comparison with that of COS. The cases of $\bar{Q} = 100$ and 400 in Fig. 3 are considered here, corresponding to the maximum ranges of 8 m and 33 m, respectively. From Figs. 9 and 10, we see that the proposed design is robust under different maximum ranges, while COS, as predicted in Fig. 3, degrades severely when the maximum range exceeds that specified by underlying communication systems, i.e., 10 m. This demonstrates the superior flexibility of the proposed design in handling different sensing requirements.

Fig. 11 shows another flexibility of the proposed design from introducing $\bar{Q}$. We see that, in overall, the detecting performance of the proposed design becomes better as $\bar{Q}$ increases. This is consistent with the SINR results observed in Figs. 4 and 5. We also see that for the low SNR shown in Fig. 11(a), the impact of $\bar{Q}$ is more prominent compared with that in the high SNR case shown in Fig. 11(b). This is reasonable as $\bar{Q}$ is introduced to increase the number of sub-blocks, and hence the SINR in the RDM. However, such improvement is limited as the larger $\bar{Q}$, the higher correlation of the IN background over sub-blocks, as illustrated in Section IV-A.

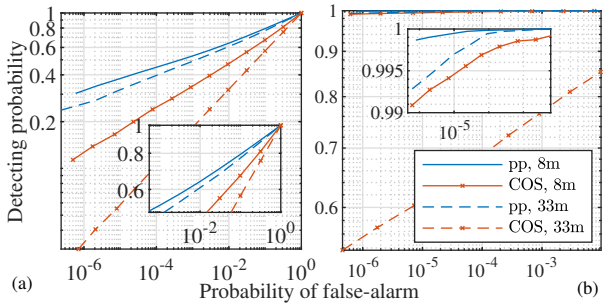

Fig. 9: Comparing the receiver operating characteristic (ROC) of COS and the proposed (pp) sensing framework using the ratio-based RDM, where $\gamma_0 = -15$ dB is set for Fig. 9(a) and $\gamma_0 = 15$ dB for Fig. 9(b). In the legend, 8 m and 33 m are the maximum ranges of targets.

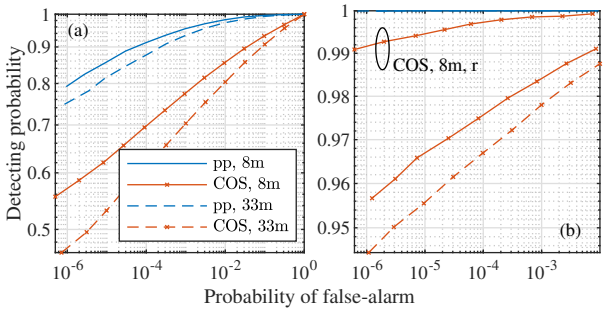

Fig. 10: ROC curves under the CCC-based RDMs, corresponding to Fig. 9. The one labeled 'COS, 8m, r' is copied from Fig. 9(b) for comparison.

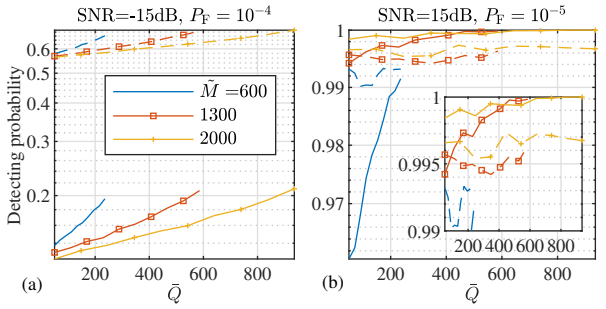

Fig. 11: Illustration of the detecting probability versus $\bar{Q}$ corresponding to the results presented in Figs. 4 and 5. The solid curves are for the ratio-based RDMs while the dash ones are for the CCC-based RDMs.

VI. Conclusions

In this paper, we develop a novel sensing framework that is applicable to not only cyclic prefixed waveforms, e.g., OFDM and DFT-S-OFDM, but also those with reduced CP, e.g., RCP-OTFS. Unlike COS and its variants, we do not follow the underlying communication system and unprecedentedly achieves the flexibility of adapting for different sensing needs. This is achieved by a new block segmentation design that segments a whole block of echo signal evenly into multiple sub-blocks that can overlap between adjacent ones. This is also accomplished by a newly introduced VCP that allows us to attain the ratio- and CCC-based RDMs under any block segmentation. We prove that the IN terms in both RDMs approximately conform to centered Gaussian distributions whose variances are also derived. We further perform a comprehensive analysis comparing COS and the proposed sensing framework as well as the sensing performance under the two types of RDMs. Extensive simulations validate the flexibility of the proposed sensing framework and its superiority over COS and C-COS.

In this work, for illustration clarity and simplicity, we have ignored the potential impact of practical transceiver on the performance of the proposed sensing framework. In particular, as seen from Fig. 1, a copy of $\tilde{s}[i]$, the time-domain transmitted communication signal, is shared with the sensing receiver before being processed by the RF chain. However, for the sensing echo signals, $\tilde{s}[i]$ would go through the transmitter RF chain and the receiver one. No two RF chains can be identical for sure. Thus, directly using $\tilde{s}[i]$ for sensing can cause performance loss. (We would mention that this seems to be a common problem in published ISAC works of similar kind.) It is interesting and important to further explore how these practical hardware factors will affect the sensing performance.

Appendix

A. Proof of Lemma 1

As illustrated in Remark 1, $s_n[l] \sim \mathcal{CN}(0, \sigma_d^2)$ and $s_n[l]$ $(\forall n)$ is i.i.d. over l. As the unitary DFT of $s_n[l]$, $S_n[m]$ $(\forall n)$ conforms to the same distribution and is i.i.d. over m. Likewise, the distribution of $W_n[m]$, which is the unitary DFT of $w_n[l]$ given in (13), conforms to a complex Gaussian distribution and is i.i.d. over m. Since $w_n[l]$ $(\forall n)$ has the non-identical variance over l, the variance of $W_n[m]$ is not equal to that of $w_n[l]$ and instead can be calculated, based on (13) and (14); specifically

$$\left(2\sigma_w^2\tilde{Q} + \sigma_w^2(\tilde{M} - \tilde{Q})\right)\Big/\tilde{M} = \left(1 + \tilde{Q}/\tilde{M}\right)\sigma_w^2.$$

Next, we analyze the distribution of $Z_n[m]$. From (14), we see that the core of $Z_n[m]$ is the DFT (w.r.t. l) of $z_n^{(p)}[l]g_{\tilde{Q}}[l]$ $(\forall p)$. From Fig. 1, we see that for any p, $z_n^{(p)}[l]g_{\tilde{Q}}[l]$ consists of two parts, one from the essential signal of the previous sub-block and the other from the sequential. Thus, $z_n^{(p)}[l]g_{\tilde{Q}}[l]$ $(\forall p,\ \forall n)$ satisfies $z_n^{(p)}[l]g_{\tilde{Q}}[l] \sim \mathcal{CN}(0, \sigma_d^2)$, is i.i.d. over l, and is independent from $s_n[l]$. As a result, the DFT of $z_n^{(p)}[l]g_{\tilde{Q}}[l]$ conforms to

$$\sum_{l=0}^{\tilde{M}-1} z_n^{(p)}[l]g_{\tilde{Q}}[l]\mathcal{Z}_{\tilde{M}}^{lm} \sim \mathcal{CN}(0, \tilde{Q}\sigma_d^2/\tilde{M}).$$

With the assumption that α_p is independent over p, the p-related summation in (14) leads to the final distribution of $Z_n[m]$ given in the statement of the lemma.

B. Proof of Lemma 2

The first statement of the lemma arises from the fact that $W_n[m]$ is only related to the receiver noise while the other two components to the essential signals. Next, we illustrate the independence of $S_n[m]$ over n.

Using the expression of $S_n[m]$ given in (14), we can have

$$\mathbb{E}\left\{S_n[m]S_{n+1}^*[m]\right\} = \mathbb{E}\left\{\left(\sum_{l_1=0}^{\tilde{M}-1} s_n[l_1]\mathcal{Z}_{\tilde{M}}^{l_1 m}\right)\times \left(\sum_{l_2=0}^{\tilde{M}-1} s_{n+1}^*[l_2]\mathcal{Z}_{\tilde{M}}^{-l_2 m}\right)\right\} = \bar{Q}\sigma_d^2 e^{-\mathrm{j}\frac{2\pi(\tilde{M}-\bar{Q})}{\tilde{M}}}\Big/\tilde{M}. \quad (39)$$

The last result is based on two facts: *First*, only at the indexes given in (40), we can have non-zero expectation; otherwise the summands involved are uncorrelated.

$$l_1 = \tilde{M} - \bar{Q}, \cdots, \tilde{M} - 1 \text{ and } l_2 = l_1 - (\tilde{M} - \bar{Q}) \quad (40)$$

Second, from Fig. 1, we can see that at the indexes given in (40), $s_n[l_1] = s_{n+1}[l_2]$. Based on (39), we can validate $\mathbb{E}\left\{|S_n[m]|^2\right\} = \sigma_d^2$ and $\mathbb{E}\left\{|S_{n+1}[m]|^2\right\} = \sigma_d^2$. Combining these expectations with (39), the correlation coefficient between $S_n[m]$ and $S_{n+1}[m]$ can be obtained, as given in the statement of Lemma 2. Following the above analysis procedure for $S_n[m]$, we can similarly calculate the correlation coefficient between $W_n[m]$ and $W_{n+1}[m]$. For brevity, we suppress the details here.

C. Proof of Lemma 3

As said in Appendix A, $S_n[m]$ $(\forall n)$ is the unitary DFT (w.r.t. l) of $s_n[l]$ that is i.i.d. over l. Thus, $S_n[m]$ $(\forall n)$ is i.i.d. over m. For the same reason, $W_n[m]$ $(\forall n)$ is i.i.d. over m. However, $Z_n[m]$ is not i.i.d. over m, since the length of $z_n^{(p)}[l] g_{\tilde{Q}}[l]$ $(\forall p)$ is smaller than the DFT dimension. Using the expression of $Z_n[m]$ given in (14), we can calculate the correlation coefficient between $Z_n[m_1]$ and $Z_n[m_2]$. Specifically, we have

$$\mathbb{E}\left\{Z_n[m_1]Z_n^*[m_2]\right\} \overset{(a)}{=} \sigma_P^2 \mathbb{E}\left\{\left(\sum_{l_1=0}^{\tilde{M}-1} z_n^{(p)}[l_1] g_{\tilde{Q}}[l_1] \mathcal{Z}_{\tilde{M}}^{l_1 m_1}\right) \times \left(\sum_{l_2=0}^{\tilde{M}-1} z_n^{(p)}[l_2] g_{\tilde{Q}}[l_2] \mathcal{Z}_{\tilde{M}}^{l_2 m_2}\right)^*\right\} \overset{(b)}{=} \sigma_P^2 \sigma_d^2 \frac{\sum_{l=0}^{\tilde{Q}-1} \mathcal{Z}_{\tilde{M}}^{l(m_1-m_2)}}{\sqrt{\tilde{M}}}, \quad (41)$$

where $\sigma_P^2 = \sum_{p=0}^{P-1} \sigma_p^2$, $\overset{(a)}{=}$ is obtained based on the uncorrelated α_p $(\forall p)$, and $\overset{(b)}{=}$ is due to to the independence of $z_n^{(p)}[l] g_{\tilde{Q}}[l]$ over l. Calculating the l-related summation on the RHS of $\overset{(b)}{=}$ by plugging in the definition of the DFT basis given in (3), we can obtain the following correlation coefficient

$$\frac{\left|\mathbb{E}\left\{Z_n[m_1]Z_n^*[m_2]\right\}\right|}{\sqrt{\mathbb{E}\left\{|Z_n[m_1]|^2\right\}\mathbb{E}\left\{|Z_n[m_2]|^2\right\}}} = \left|f(m_1 - m_2)\right|, \quad (42)$$
$$\text{s.t. } f(m_1 - m_2) = \sin\left(\tfrac{2\pi}{\tilde{M}} \tfrac{\tilde{Q}(m_1-m_2)}{2}\right) \Big/ \left(\tilde{Q} \sin\left(\tfrac{2\pi}{\tilde{M}} \tfrac{(m_1-m_2)}{2}\right)\right)$$

where $\mathbb{E}\left\{|Z_n[m_1]|^2\right\}$ can be readily attained by setting $m_2 = m_1$ in (41); likewise for $\mathbb{E}\left\{|Z_n[m_2]|^2\right\}$.

D. Proof of Proposition 1

As said above (27), with a sufficiently large g introduced, $|\mathsf{g} S_n[m]| < 1$ can barely happen. Moreover, the operator $\mathbb{I}_{\mathcal{E}}\{\cdot\}$ fully removes the cases of $|\mathsf{g} S_n[m]| < 1$. Therefore, we have

$$\left|D_{n,m}^{k,l} / \mathsf{g} S_n[m]\right| \le \max\left\{\left|\mathsf{g} D_{n,m}^{k,l} S_n^*[m]\right|\right\}, \quad (43)$$

where $D_{n,m}^{k,l}$ is defined in (24). Since $D_{n,m}^{k,l}/\mathsf{g} S_n[m]$ conforms to a truncated Cauchy distribution, we are now able to invoke the CLT on deriving the distribution of $\tilde{W}_k^{\mathrm{r}}[l] + \tilde{Z}_k^{\mathrm{r}}[l]$. Based on Lemma 2, we know that $Z_n[m]$ is independent over n and, under the condition $\tilde{M} \gg (\tilde{Q} + \bar{Q})$, such independence is also owned by $S_n[m]$ and $W_n[m]$. Accordingly, the ratio $D_{n,m}^{k,l}/\mathsf{g} S_n[m]$ $(\forall m)$ is independent over n. Invoking the CLT under large $\tilde{N}$, we attain

$$\sum_{n=0}^{\tilde{N}-1} \frac{D_{n,m}^{k,l}}{\mathsf{g} S_n[m]} \sim \mathcal{CN}\left(0, \tilde{N}\left(\rho \mathsf{b}(\epsilon)\right)\right), \quad (44)$$
$$\text{s.t. } \rho = \frac{(\sigma_Z^2 + \sigma_W^2)}{\tilde{M}\tilde{N}\mathsf{g}^2\sigma_d^2},\ b(\epsilon) = 2\left(\ln\left(\frac{2(1-\epsilon)}{\sqrt{\epsilon(2-\epsilon)}}\right) - 1\right),$$

where ϵ is a sufficiently small value and $\rho\mathsf{b}(\epsilon)$ is the variance of each summand according to [37, Proposition 1]. Note that ρ is the ratio between the variance of $D_{2\tilde{n},m}^{k,l}$, as given in (25), and that of $\mathsf{g} S_{2\tilde{n}}[m]$, as easily deduced from Lemma 1.

With (44) attained, we know that $\tilde{W}_k^{\mathrm{r}}[l] + \tilde{Z}_k^{\mathrm{r}}[l]$ also conforms to a Gaussian distribution, as it is the summation of $\sum_{n=0}^{\tilde{N}-1} \frac{D_{n,m}^{k,l}}{\mathsf{g} S_n[m]}$ over m. Moreover, as shown below, $\sum_{n=0}^{\tilde{N}-1} \frac{D_{n,m}^{k,l}}{\mathsf{g} S_n[m]}$ is approximately independent over m. This leads to the final distribution of $\tilde{W}_k^{\mathrm{r}}[l] + \tilde{Z}_k^{\mathrm{r}}[l]$, as given in the statement of Proposition 1.

Independence of $\sum_{n=0}^{\tilde{N}-1} \frac{D_{n,m}^{k,l}}{\mathsf{g} S_n[m]}$ over m: As Gaussian-distributed, $\sum_{n=0}^{\tilde{N}-1} \frac{D_{n,m_1}^{k,l}}{\mathsf{g} S_n[m_1]}$ and $\sum_{n=0}^{\tilde{N}-1} \frac{D_{n,m_2}^{k,l}}{\mathsf{g} S_n[m_2]}$ are independent if they are uncorrelated. Replacing $D_{n,m}^{k,l}$ with its full expression given in (24), we can have

$$\begin{aligned}
&\mathbb{E}\left\{\left(\sum_{n_1=0}^{\tilde{N}-1} \frac{(Z_{n_1}[m_1] + W_{n_1}[m_1]) \mathcal{Z}_{\tilde{M}}^{-m_1 l} \mathcal{Z}_{\tilde{N}}^{n_1 k}}{\mathsf{g} S_{n_1}[m_1]}\right) \times \left(\sum_{n_2=0}^{\tilde{N}-1} \frac{(Z_{n_2}[m_2] + W_{n_2}[m_2]) \mathcal{Z}_{\tilde{M}}^{-m_2 l} \mathcal{Z}_{\tilde{N}}^{n_2 k}}{\mathsf{g} S_{n_2}[m_2]}\right)^*\right\} \\
&\overset{(a)}{=} \mathbb{E}\left\{\sum_{n=0}^{\tilde{N}-1} \frac{(Z_n[m_1] + W_n[m_1])(Z_n^*[m_2] + W_n^*[m_2]) e^{\mathrm{j}\frac{2\pi l(m_1-m_2)}{\tilde{M}}}}{\mathsf{g}^2 S_n[m_1] S_n^*[m_2] \tilde{N}\tilde{M}}\right\} \\
&= \sum_{n=0}^{\tilde{N}-1} \mathbb{E}\left\{f/g\right\} \overset{(b)}{\approx} \sum_{n=0}^{\tilde{N}-1} \mu_f/\mu_g = 0, \\
&\text{s.t. } f = \left(Z_n[m_1]Z_n^*[m_2] + Z_n[m_1]W_n^*[m_2] + W_n[m_1]Z_n^*[m_2] + W_n[m_1]W_n^*[m_2]\right) S_n^*[m_1] S_n[m_2] e^{\mathrm{j}\frac{2\pi l(m_1-m_2)}{\tilde{M}}} \\
&\quad g = \mathsf{g}^2 |S_n[m_1] S_n[m_2]|^2 \tilde{N}\tilde{M}, \quad (45)
\end{aligned}$$

where $\overset{(a)}{=}$ is obtained by suppressing all cross-terms at $n_1 \neq n_2$ since they are uncorrelated; and $\overset{(b)}{\approx}$ is attained by applying the first-order approximation of the mean of the ratio f/g [43]. The last result is based on $\mu_f = 0$ which can be readily obtained by applying Lemmas 2 and 3.

E. Proof of Proposition 2

Consider $S_k^{\mathrm{c}}[l]$ first. According to Lemma 1, we have $S_n[m] \sim \mathcal{CN}(0, \sigma_d^2)$. This then yields $\frac{|S_n[m]|^2}{\sigma_d^2/2} \sim \chi_2^2$ and

$$\mathbb{E}\left\{\frac{|S_n[m]|^2}{\sigma_d^2/2}\right\} = 2,\ \mathbb{V}\left\{\frac{|S_n[m]|^2}{\sigma_d^2/2}\right\} = 4, \quad (46)$$

where χ_2^2 denotes the chi-square distribution with two degrees of freedom (DoF). Given that $S_n[m]$ $(\forall n)$ is statistically

independent of m, we first consider the m-related summation in calculating $S_k^{\mathrm{c}}[l]$; see (16). Invoking the CLT, we know that the summation leads to a Gaussian distribution whose variance is given by

$$\mathbb{V}\left\{\frac{\sigma_d^2}{2}\sum_{m=0}^{\tilde{M}-1}\frac{|S_n[m]|^2}{\sigma_d^2/2}e^{-\mathrm{j}\frac{2\pi m \mathsf{l}_p}{\tilde{M}}}\mathcal{Z}_{\tilde{M}}^{-ml}\right\}=\sigma_d^4.$$

The mean of the Gaussian distribution is more complicated, as we need to consider the cases of $l=\mathsf{l}_p$ and $l\neq\mathsf{l}_p$. For the first case, we have

$$\mathbb{E}\left\{\frac{\sigma_d^2}{2}\sum_{m=0}^{\tilde{M}-1}\frac{|S_n[m]|^2}{\sigma_d^2/2}e^{-\mathrm{j}\frac{2\pi m \mathsf{l}_p}{\tilde{M}}}\mathcal{Z}_{\tilde{M}}^{-m\mathsf{l}_p}\right\}=\sigma_d^2\sqrt{\tilde{M}},$$

where $e^{-\mathrm{j}\frac{2\pi m \mathsf{l}_p}{\tilde{M}}}\mathcal{Z}_{\tilde{M}}^{-m\mathsf{l}_p}=1/\sqrt{\tilde{M}}$ is applied. For the case of $l\neq\mathsf{l}_p$, we have

$$\begin{aligned}\mathbb{E}\left\{\frac{\sigma_d^2}{2}\sum_{m=0}^{\tilde{M}-1}\frac{|S_n[m]|^2}{\sigma_d^2/2}e^{-\mathrm{j}\frac{2\pi m \mathsf{l}_p}{\tilde{M}}}\mathcal{Z}_{\tilde{M}}^{-ml}\right\}&=\sigma_d^2\sum_{m=0}^{\tilde{M}-1}e^{\mathrm{j}\frac{2\pi m(l-\mathsf{l}_p)}{\tilde{M}}}\\&=0,\end{aligned}\tag{47}$$

where we have applied the fact that summing a discrete single-tone exponential signal (with a non-zero frequency) over integer cycles leads to zero. Combining the above discussion, we conclude

$$\sum_{m=0}^{\tilde{M}-1}|S_n[m]|^2e^{-\mathrm{j}\frac{2\pi m \mathsf{l}_p}{\tilde{M}}}\mathcal{Z}_{\tilde{M}}^{-ml}\sim\begin{cases}\mathcal{N}\left(\sigma_d^2\sqrt{\tilde{M}},\sigma_d^4\right) & l=\mathsf{l}_p\\ \mathcal{N}\left(0,\sigma_d^4\right) & l\neq\mathsf{l}_p\end{cases}.$$

Based on Lemma 2, $\sum_{m=0}^{\tilde{M}-1}|S_n[m]|^2e^{-\mathrm{j}\frac{2\pi m \mathsf{l}_p}{\tilde{M}}}\mathcal{Z}_{\tilde{M}}^{-ml}$ is independent over the set of either odd n or even n, but shows dependence between adjacent pair. However, under the assumption of $\tilde{M}\gg(\tilde{Q}+\bar{Q})$, the dependence is weak as the correlation coefficient approaches zero. Thus, summing the LHS of the above equation over n converges in distribution to another Gaussian with its statistical properties depicted in the statement of Proposition 2. The distribution of $\mathsf{X}_k^{\mathrm{r}}[l]$, $\mathsf{X}\in\{W,Z\}$ can be similarly derived with reference to Appendix D. Thus, we suppress the details for brevity.

REFERENCES

[1] F. Liu, C. Masouros, A. P. Petropulu, H. Griffiths, and L. Hanzo, "Joint radar and communication design: Applications, state-of-the-art, and the road ahead," *IEEE Trans. Commun.*, vol. 68, no. 6, pp. 3834–3862, 2020.

[2] A. Hassanien, M. G. Amin, E. Aboutanios, and B. Himed, "Dual-function radar communication systems: A solution to the spectrum congestion problem," *IEEE Signal Process. Mag.*, vol. 36, no. 5, pp. 115–126, Sep. 2019.

[3] D. Ma, N. Shlezinger, T. Huang, Y. Liu, and Y. C. Eldar, "Joint radar-communication strategies for autonomous vehicles: Combining two key automotive technologies," *IEEE Signal Process. Mag.*, vol. 37, no. 4, pp. 85–97, 2020.

[4] K. V. Mishra, M. B. Shankar, V. Koivunen, B. Ottersten, and S. A. Vorobyov, "Toward millimeter-wave joint radar communications: A signal processing perspective," *IEEE Signal Process. Mag.*, vol. 36, no. 5, pp. 100–114, 2019.

[5] K. Wu, J. A. Zhang, X. Huang, and Y. J. Guo, "Frequency-hopping MIMO radar-based communications: An overview," *IEEE Aerosp. Electron. Syst. Mag.*, pp. 1–1, early access, 2021.

[6] P. Kumari, J. Choi, N. González-Prelcic, and R. W. Heath, "IEEE 802.11ad-based radar: An approach to joint vehicular communication-radar system," *IEEE Trans. Vehic. Techn.*, pp. 67(4) 3012–3027, 2018.

[7] E. Grossi, M. Lops, L. Venturino, and A. Zappone, "Opportunistic radar in IEEE 802.11ad networks," *IEEE Trans. Signal Process.*, vol. 66, no. 9, pp. 2441–2454, May 2018.

[8] G. Duggal, S. Vishwakarma, K. V. Mishra, and S. S. Ram, "Doppler-resilient 802.11 ad-based ultrashort range automotive joint radar-communications system," *IEEE Trans. Aerospace Electr. Syst.*, vol. 56, no. 5, pp. 4035–4048, 2020.

[9] Q. Zhang, H. Sun, Z. Wei, and Z. Feng, "Sensing and communication integrated system for autonomous driving vehicles," in *IEEE INFOCOM WKSHPS*, 2020, pp. 1278–1279.

[10] C. Sturm and W. Wiesbeck, "Waveform design and signal processing aspects for fusion of wireless communications and radar sensing," *Proc. IEEE*, vol. 99, no. 7, pp. 1236–1259, 2011.

[11] Y. Zeng, Y. Ma, and S. Sun, "Joint radar-communication with cyclic prefixed single carrier waveforms," *IEEE Trans. Veh. Techn.*, vol. 69, no. 4, pp. 4069–4079, 2020.

[12] T. Wild, V. Braun, and H. Viswanathan, "Joint design of communication and sensing for beyond 5G and 6G systems," *IEEE Access*, vol. 9, pp. 30 845–30 857, 2021.

[13] C. B. Barneto, S. D. Liyanaarachchi, T. Riihonen, L. Anttila, and M. Valkama, "Multibeam design for joint communication and sensing in 5G new radio networks," in *2020 ICC*, 2020, pp. 1–6.

[14] F. Liu, Y.-F. Liu, A. Li, C. Masouros, and Y. C. Eldar, "Cramér-rao bound optimization for joint radar-communication design," *arXiv preprint arXiv:2101.12530*, 2021.

[15] S. H. Dokhanchi, M. R. B. Shankar, M. Alaee-Kerahroodi, and B. Ottersten, "Adaptive waveform design for automotive joint radar-communication systems," *IEEE Trans. Veh. Technol.*, vol. 70, no. 5, pp. 4273–4290, 2021.

[16] A. R. Chiriyath, S. Ragi, H. D. Mittelmann, and D. W. Bliss, "Novel radar waveform optimization for a cooperative radar-communications system," *IEEE Trans Aerosp Electron Syst*, vol. 55, no. 3, pp. 1160–1173, 2019.

[17] J. A. Zhang, F. Liu, C. Masouros, R. W. Heath, Z. Feng, L. Zheng, and A. Petropulu, "An overview of signal processing techniques for joint communication and radar sensing," *IEEE J. Sel. Top. Signal Process*, vol. 15, no. 6, pp. 1295–1315, 2021.

[18] J. A. Zhang, M. L. Rahman, K. Wu, X. Huang, Y. J. Guo, S. Chen, and J. Yuan, "Enabling joint communication and radar sensing in mobile networks -a survey," *IEEE Commun. Surv. Tutor.*, pp. 1–1, early access, 2021.

[19] Z. Wei, F. Liu, C. Masouros, N. Su, and A. P. Petropulu, "Towards multi-functional 6G wireless networks: Integrating sensing, communication and security," *arXiv preprint arXiv:2107.07735*, 2021.

[20] Y. Cui, F. Liu, X. Jing, and J. Mu, "Integrating sensing and communications for ubiquitous iot: Applications, trends, and challenges," *IEEE Network*, vol. 35, no. 5, pp. 158–167, 2021.

[21] F. Roos, J. Bechter, C. Knill, B. Schweizer, and C. Waldschmidt, "Radar sensors for autonomous driving: Modulation schemes and interference mitigation," *IEEE Microw. Mag.*, vol. 20, no. 9, pp. 58–72, 2019.

[22] G. Hakobyan and B. Yang, "High-performance automotive radar: A review of signal processing algorithms and modulation schemes," *IEEE Signal Process. Mag.*, vol. 36, no. 5, pp. 32–44, 2019.

[23] Z. Wei, W. Yuan, S. Li, J. Yuan, G. Bharatula, R. Hadani, and L. Hanzo, "Orthogonal time-frequency space modulation: A full-diversity next generation waveform," *arXiv preprint arXiv:2010.03344*, 2020.

[24] L. Gaudio, M. Kobayashi, G. Caire, and G. Colavolpe, "On the effectiveness of OTFS for joint radar parameter estimation and communication," *IEEE Trans. Wireless Commun.*, vol. 19, no. 9, pp. 5951–5965, 2020.

[25] W. Yuan, Z. Wei, S. Li, J. Yuan, and D. W. K. Ng, "Integrated sensing and communication-assisted orthogonal time frequency space transmission for vehicular networks," *IEEE J. Sel. Top. Signal Process*, vol. 15, no. 6, pp. 1515–1528, 2021.

[26] P. Raviteja, K. T. Phan, and Y. Hong, "Embedded pilot-aided channel estimation for OTFS in delay–doppler channels," *IEEE Trans. Veh. Techn.*, vol. 68, no. 5, pp. 4906–4917, 2019.

[27] M. F. Keskin, H. Wymeersch, and A. Alvarado, "Radar sensing with OTFS: Embracing ISI and ICI to surpass the ambiguity barrier," *arXiv preprint arXiv:2103.16162*, 2021.

[28] Z. Wei, W. Yuan, S. Li, J. Yuan, and D. W. K. Ng, "Transmitter and receiver window designs for orthogonal time-frequency space modulation," *IEEE Trans. Commun.*, vol. 69, no. 4, pp. 2207–2223, 2021.

[29] S. S. Das, V. Rangamgari, S. Tiwari, and S. C. Mondal, "Time domain channel estimation and equalization of CP-OTFS under multiple fractional dopplers and residual synchronization errors," *IEEE Access*, vol. 9, pp. 10 561–10 576, 2021.

[30] P. Raviteja, Y. Hong, E. Viterbo, and E. Biglieri, "Practical pulse-shaping waveforms for reduced-cyclic-prefix OTFS," *IEEE Trans. Veh. Techn.*, vol. 68, no. 1, pp. 957–961, 2019.

[31] S. Wei, D. L. Goeckel, and P. A. Kelly, "Convergence of the complex envelope of bandlimited OFDM signals," *IEEE Trans. Information Theory*, vol. 56, no. 10, pp. 4893–4904, 2010.

[32] A. V. Oppenheim, *Discrete-time signal processing*. Pearson Education India, 1999.

[33] M. A. Richards, J. Scheer, W. A. Holm, and W. L. Melvin, *Principles of modern radar*. Citeseer, 2010.

[34] S. Ahmadi, *5G NR: Architecture, Technology, Implementation, and Operation of 3GPP New Radio Standards*. Academic Press, 2019.

[35] H. L. Van Trees, *Optimum array processing: Part IV of detection, estimation, and modulation theory*. John Wiley & Sons, 2004.

[36] K. Wu, J. A. Zhang, X. Huang, and Y. J. Guo, "Accurate frequency estimation with fewer dft interpolations based on padé approximation," *IEEE Trans. Veh. Techn.*, vol. 70, no. 7, pp. 7267–7271, 2021.

[37] ——, "Otfs-based joint communication and sensing for future industrial iot," *IEEE Internet of Things Journal*, pp. 1–1, early access, 2021.

[38] ——, "A low-complexity method for FFT-based OFDM sensing," *arXiv preprint arXiv:2105.13596*, 2021.

[39] M. Kronauge and H. Rohling, "Fast two-dimensional cfar procedure," *IEEE Trans. Aerospace Electr. Syst.*, vol. 49, no. 3, pp. 1817–1823, 2013.

[40] R. J. Baxley, B. T. Walkenhorst, and G. Acosta-Marum, "Complex gaussian Ratio distribution with applications for error rate calculation in fading channels with imperfect csi," in *2010 IEEE Global Telecommunications Conference GLOBECOM 2010*, 2010, pp. 1–5.

[41] F. Hampel and E. Zurich, "Is statistics too difficult?" *Canadian Journal of Statistics*, vol. 26, no. 3, pp. 497–513, 1998.

[42] N. O'Donoughue and J. M. F. Moura, "On the product of independent complex Gaussians," *IEEE Trans. Signal Process.*, vol. 60, no. 3, pp. 1050–1063, 2012.

[43] H. Seltman, "Approximations for mean and variance of a ratio," *unpublished note*, 2012.

Kai Wu received the B.E. from Xidian University, Xi'an, China, in 2012, PhD from Xidian University in 2019, and PhD from the University of Technology Sydney (UTS), Sydney, Australia, in 2020. He is now a research fellow at the Global Big Data Technologies Centre, UTS. From Nov. 2017 to April 2018, he was a research assistant at the same centre. Before that, he was a visiting scholar at DATA61, CSIRO, Australia (Nov. 2016 - Nov. 2017). His research interests include array signal processing, and its applications in radar and communications.

Dr J. Andrew Zhang (M'04-SM'11) received the B.Sc. degree from Xi'an JiaoTong University, China, in 1996, the M.Sc. degree from Nanjing University of Posts and Telecommunications, China, in 1999, and the Ph.D. degree from the Australian National University, in 2004.

Currently, Dr. Zhang is an Associate Professor in the School of Electrical and Data Engineering, University of Technology Sydney, Australia. He was a researcher with Data61, CSIRO, Australia from 2010 to 2016, the Networked Systems, NICTA, Australia from 2004 to 2010, and ZTE Corp., Nanjing, China from 1999 to 2001. Dr. Zhang's research interests are in the area of signal processing for wireless communications and sensing. He has published more than 200 papers in leading international Journals and conference proceedings, and has won 5 best paper awards. He is a recipient of CSIRO Chairman's Medal and the Australian Engineering Innovation Award in 2012 for exceptional research achievements in multi-gigabit wireless communications.

Xiaojing Huang (M'99-SM'11) received the B.Eng., M.Eng., and Ph.D. degrees in electronic engineering from Shanghai Jiao Tong University, Shanghai, China, in 1983, 1986, and 1989, respectively. He was a Principal Research Engineer with the Motorola Australian Research Center, Botany, NSW, Australia, from 1998 to 2003, and an Associate Professor with the University of Wollongong, Wollongong, NSW, Australia, from 2004 to 2008. He had been a Principal Research Scientist with the Commonwealth Scientific and Industrial Research Organisation (CSIRO), Sydney, NSW, Australia, and the Project Leader of the CSIRO Microwave and mm-Wave Backhaul projects since 2009. He is currently a Professor of Information and Communications Technology with the School of Electrical and Data Engineering and the Program Leader for Mobile Sensing and Communications with the Global Big Data Technologies Center, University of Technology Sydney (UTS), Sydney, NSW, Australia. His research interests include high-speed wireless communications, digital and analog signal processing, and synthetic aperture radar imaging. With over 32 years of combined industrial, academic, and scientific research experience, he has authored over 330 book chapters, refereed journal and conference papers, major commercial research reports, and filed 31 patents. Prof. Huang was a recipient of the CSIRO Chairman's Medal and the Australian Engineering Innovation Award in 2012 for exceptional research achievements in multigigabit wireless communications.

Y. Jay Guo (Fellow'2014) received a Bachelor Degree and a Master Degree from Xidian University in 1982 and 1984, respectively, and a PhD Degree from Xian Jiaotong University in 1987, all in China. His research interest includes antennas, mm-wave and THz communications and sensing systems as well as big data technologies. He has published four books and over 550 research papers including 300 journal papers, most of which are in IEEE Transactions, and he holds 26 patents. He is a Fellow of the Australian Academy of Engineering and Technology, a Fellow of IEEE and a Fellow of IET, and was a member of the College of Experts of Australian Research Council (ARC, 2016-2018). He has won a number of most prestigious Australian Engineering Excellence Awards (2007, 2012) and CSIRO Chairman's Medal (2007, 2012). He was named one of the most influential engineers in Australia in 2014 and 2015, respectively, and one of the top researchers in Australia in 2020.

Currently, he is a Distinguished Professor and the Director of Global Big Data Technologies Centre (GBDTC) at the University of Technology Sydney (UTS), Australia. Prior to this appointment in 2014, he served as a Director in CSIRO for over nine years. Before joining CSIRO, he held various senior technology leadership positions in Fujitsu, Siemens and NEC in the U.K.

Prof Guo has chaired numerous international conferences and served as guest editors for a number of IEEE publications. He is the Chair of International Steering Committee, International Symposium on Antennas and Propagation (ISAP). He was the International Advisory Committee Chair of IEEE VTC2017, General Chair of ISAP2022, ISAP2015, iWAT2014 and WPMC'2014, and TPC Chair of 2010 IEEE WCNC, and 2012 and 2007 IEEE ISCIT. He served as Guest Editor of special issues on "Low-Cost Wide-Angle Beam Scanning Antennas", "Antennas for Satellite Communications" and "Antennas and Propagation Aspects of 60-90GHz Wireless Communications," all in IEEE Transactions on Antennas and Propagation, Special Issue on "Communications Challenges and Dynamics for Unmanned Autonomous Vehicles," IEEE Journal on Selected Areas in Communications (JSAC), and Special Issue on "5G for Mission Critical Machine Communications", IEEE Network Magazine.